AD-A065 586   OHIO STATE UNIV COLUMBUS ELECTROSCIENCE LAB   F/G 9/5

HIGH FREQUENCY NEAR FIELD SCATTERING BY AN ELLIPTIC DISK.(U)

DEC 76   E D GREER, W D BURNSIDE   N62269-76-C-0554

UNCLASSIFIED   ESL-4583-1   NADC-79041-30   NL

| OF |

AD
AO 65586

END
DATE
FILMED

5--79

DDC

HIGH FREQUENCY NEAR FIELD SCATTERING BY AN ELLIPTIC DISK
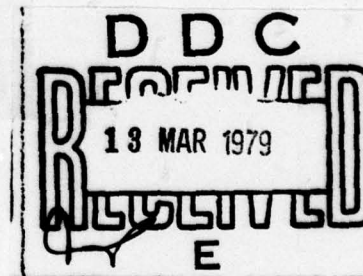
Eric D. Greer and W. D. Burnside

REPORT DOCUMENTATION PAGE		READ INSTRUCTIONS BEFORE COMPLETING FORM
1. REPORT NUMBER NADC-79041-30	**2. GOVT ACCESSION NO.**	**3. RECIPIENT'S CATALOG NUMBER**
4. TITLE (and Subtitle) HIGH FREQUENCY NEAR FIELD SCATTERING BY AN ELLIPTIC DISK		**5. TYPE OF REPORT & PERIOD COVERED** Technical Report
		6. PERFORMING ORG. REPORT NUMBER ESL 4583-1
7. AUTHOR(s) Eric D. Greer and W. D. Burnside		**8. CONTRACT OR GRANT NUMBER(s)** Contract N62269-76-C-0554
9. PERFORMING ORGANIZATION NAME AND ADDRESS The Ohio State University ElectroScience Laboratory Department of Electrical Engineering Columbus, Ohio 43212		**10. PROGRAM ELEMENT, PROJECT, TASK AREA & WORK UNIT NUMBERS** 63206N,WR6-1154 WTW180000,RA702
11. CONTROLLING OFFICE NAME AND ADDRESS Department of the Navy Naval Air Development Center Warminster, Pennsylvania 18974		**12. REPORT DATE** December 1976
		13. NUMBER OF PAGES 59
14. MONITORING AGENCY NAME & ADDRESS(if different from Controlling Office)		**15. SECURITY CLASS. (of this report)** Unclassified
		15a. DECLASSIFICATION/DOWNGRADING SCHEDULE

16. DISTRIBUTION STATEMENT (of this Report)

Approved for public release; distribution unlimited

17. DISTRIBUTION STATEMENT (of the abstract entered in Block 20, if different from Report)

18. SUPPLEMENTARY NOTES

19. KEY WORDS (Continue on reverse side if necessary and identify by block number)

Elliptic disk
Geometrical Theory of Diffraction
Equivalent currents
Radiation patterns

20. ABSTRACT (Continue on reverse side if necessary and identify by block number)

The analysis of the high frequency radiation pattern of an antenna mounted near an elliptic disk is the object of this research. This is an analytic study of basic antenna types using GTD (ray optical) techniques. The elliptic disk is modelled as a perfectly conducting flat plate and patterns are taken in the far field. An equivalent current modification is introduced to correct caustic and pseudo-caustic regions where the GTD solution fails. The validity of the solution is shown by comparing the predicted pattern

DD FORM 1473 EDITION OF 1 NOV 65 IS OBSOLETE
1 JAN 73

20.

against measured results. The elliptic disk solution can be used to approximate antenna patterns of antenna mounted near arbitrary cross-section flat plates. This solution can also be used as part of an elliptic cylinder solution for aircraft and ship models.

ACKNOWLEDGMENTS

CONTENTS

CHAPTER I
INTRODUCTION

The object of this study is to analyze the high frequency radiated field of an antenna mounted near an elliptic disk. The elliptic disk is studied because of its generality in modelling arbitrary cross-section flat plates. The elliptic disk can be used to predict antenna patterns for antennas located on circular or elliptic ground planes. This solution can, also, be used to model an endcap of a finite elliptic cylinder used for modelling structures on aircraft such as the fuselage, engines, and stores or structures on ships such as masks, stores, etc.

The basic approach taken in this study is to employ the Geometrical Theory of Diffraction (GTD). Since GTD is a high fre-quency method the lower frequency limit of this solution is dictated by the physical dimensions of the ellipse and the source position. The radius of curvature of the ellipse should be greater than a half-wavelength and the source should be at least a half-wavelength away from the elliptic edge.

The basic problem is analyzed using Keller's Geometrical Theory of Diffraction [1] along with the more accurate and general ray diffraction coefficients developed at The Ohio State University [2]. The solution for the elliptic disk case is modified in the caustic and pseudo-caustic regions by employing the method of equivalent current developed by Ryan and Peters [3]. An empirical switching procedure is also developed in order to determine where to employ the equivalent current solution to correct these caustics to yield a uniform solution.

1

CHAPTER II
THEORETICAL BACKGROUND

A.   INTRODUCTION

The radiated field of an antenna positioned near an elliptic disk is analyzed using the Geometrical Theory of Diffraction (GTD). The GTD is a high frequency ray optic technique which allows the radiated field to be analyzed in terms of individual ray components.

In this study, the scattering body is assumed to be perfectly conducting and surrounded entirely by free space. The geometry associated with this problem is illustrated in Figure 1. All fields carry an $\exp(j\omega t)$ time dependence which is assumed and suppressed.
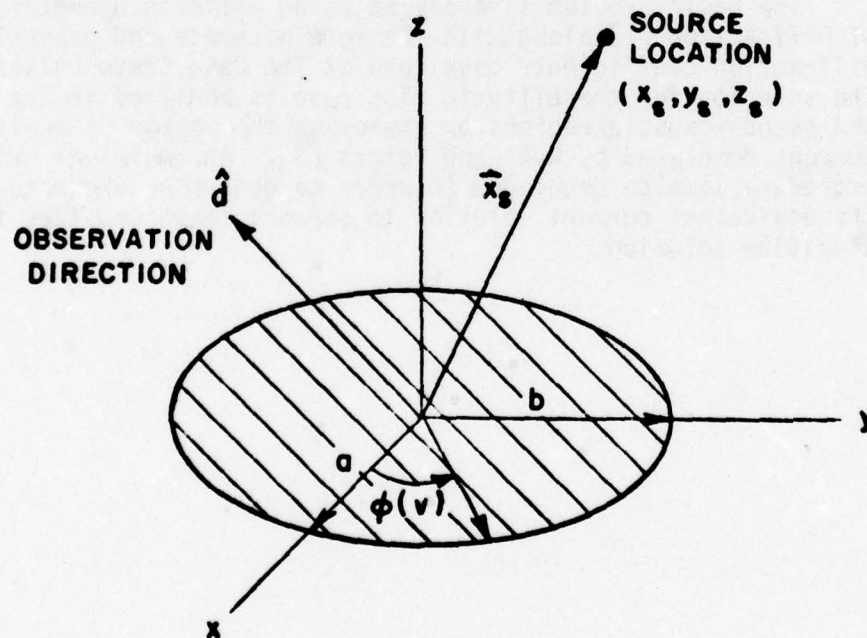
Figure 1. Elliptic disk geometry.

B.   GEOMETRICAL OPTICS FIELDS

The incident electric field $\vec{E}^i$ can be generated by an arbitrary source. In this study, electric or magnetic current moments producing a spherical wave are assumed. Note that an arbitrary source could be constructed using superposition of these current elements [4]. The far field pattern of the source is written as

$$\vec{E}^i(\theta,\phi) = [\hat{\theta} F(\theta,\phi) + \hat{\phi} G(\theta,\phi)] \frac{e^{-jks}}{s} \tag{1}$$

where $F(\theta,\phi)$ and $G(\theta,\phi)$ are the source pattern functions and s is the distance between the source and the observation point.

The reflected electric field from a perfectly conducting flat plate is determined from image theory and is expressed as

$$\vec{E}^r(\theta,\phi) = [\hat{\theta} F^r(\theta,\phi) + \hat{\phi} G^r(\theta,\phi)] \frac{e^{-jks'}}{s'} \tag{2}$$

where s' is the distance between the image source and the observation point. The geometry associated with the reflected field is shown in Figure 2.

The reflected field is determined using the source field incident on the point of reflection Q and the boundary conditions. The source field incident at Q is given by

$$\vec{E}^i(\theta_i,\phi_i) = [\hat{\theta} F(\theta_i,\phi_i) + \hat{\phi} G(\theta_i,\phi_i)] \frac{e^{-jk|\vec{I}|}}{|\vec{I}|}$$

where $|\vec{I}|$ is the distance between the source and the point of reflection and the angles θ_i and ϕ_i are the angles of incidence from the source to the point of reflection. The boundary conditions applied at Q are given by

$$\hat{z} \cdot \vec{E}^r = \hat{z} \cdot \vec{E}^i \tag{3a}$$

and

$$\hat{t} \cdot \vec{E}^r = -\hat{t} \cdot \vec{E}^i \tag{3b}$$

3
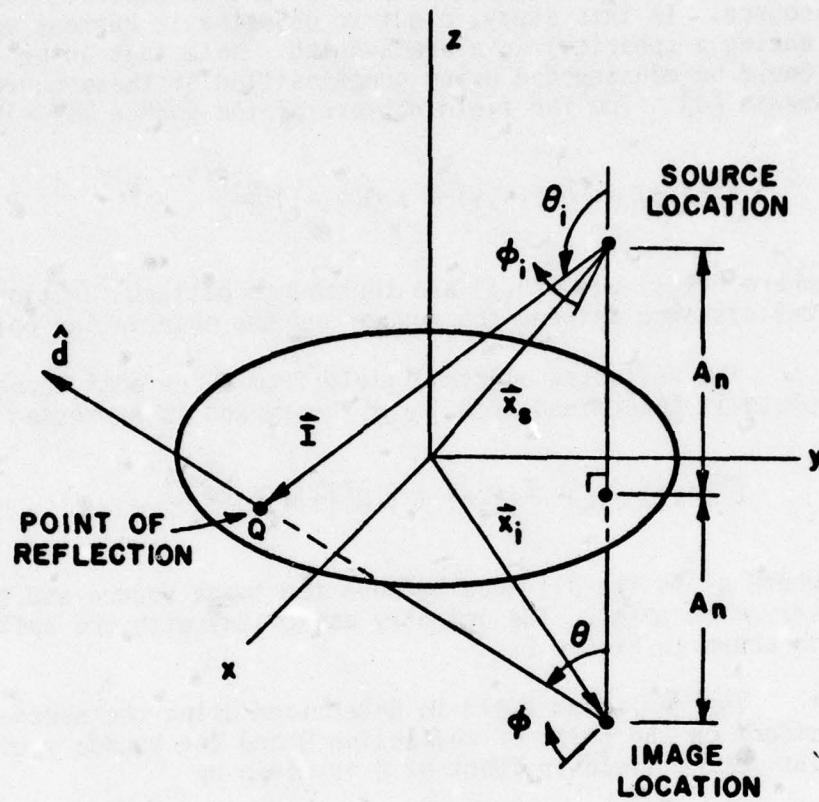
Figure 2. Geometry for reflected field.

where $\hat{z}$ is the normal to the surface and $\hat{t}$ is a tangent vector to the surface defined by

$$\hat{t} = \frac{\hat{z} \times \hat{I}}{|\hat{z} \times \hat{I}|} \quad .$$

Equations (3a) and (3b) can be rewritten as

$$(\hat{z} \cdot \hat{\theta})F^r + (\hat{z} \cdot \hat{\phi})G^r = (\hat{z} \cdot \hat{\theta}_i)F + (\hat{z} \cdot \hat{\phi}_i)G$$

$$(\hat{t} \cdot \hat{\theta})F^r + (t \cdot \hat{\phi})Gr = (-\hat{t} \cdot \hat{\theta}_i)F + (-\hat{t} \cdot \hat{\phi}_i)G \quad .$$

4

The only unknowns in the above equations are the desired functions F^r and G^r.   Solving these equations yields

$$F^r = \frac{(\hat{t} \cdot \hat{\phi})A^n + (\hat{z} \cdot \hat{\phi})A^t}{(\hat{z} \cdot \hat{\theta})(\hat{t} \cdot \hat{\phi}) - (\hat{z} \cdot \hat{\phi})(\hat{t} \cdot \hat{\theta})} \tag{4a}$$

$$G^r = \frac{-[(\hat{z} \cdot \hat{\theta})A^t + (\hat{t} \cdot \hat{\phi})A^n]}{(\hat{z} \cdot \hat{\theta})(\hat{t} \cdot \hat{\phi}) - (\hat{z} \cdot \hat{\phi})(\hat{t} \cdot \hat{\theta})} \tag{4b}$$

where

$$A^n = (\hat{z} \cdot \hat{\theta}_i)F + (\hat{z} \cdot \hat{\phi}_i)G$$

$$A^t = (\hat{t} \cdot \hat{\theta}_i)F + (\hat{t} \cdot \hat{\phi}_i)G.$$

C.   DIFFRACTION BY A WEDGE

An asymptotic solution for the diffraction from a conducting wedge was first solved by Sommerfeld [5]. Originally plane wave diffraction coefficients as presented by Keller [6] were used as the basis for the GTD solution; however, as shown in Reference [7], the use of cylindrical wave diffraction is necessary for antenna applications. Thus, different formulations for wedge diffraction were substituted for the plane wave diffraction coefficient which is the basis for wedge diffraction theory. Pauli [8] introduced the V_B function as a practical formulation for a finite angle conducting wedge. Hutchins and Kouyoumjian [9,10] have presented a formula for the diffracted field which significantly improves the accuracy of the solution over that obtained from Pauli's form. This improved solution provides superior results in the transition regions (near the incident and reflected shadow boundaries).

The three-dimensional wedge diffraction geometry is depicted in Figures 3 and 4. The source, located at $s'(\rho',\phi',z')$, generates a radiated $\bar{E}$ field given by $\bar{E}^i(s)$. The source can be an arbitrary electric or magnetic source causing cylindrical, conical or spherical wave incidence on the wedge. The diffracted vector field at $s(\rho,\phi,z)$ can be written in terms of a dyadic diffraction coefficient.

5

OBSERVATION POINT
LIT REGION
$\bar{E}^i$
SOURCE POINT
REFLECTION SHADOW BOUNDARY
$\bar{E}^d$
$\bar{E}^r$
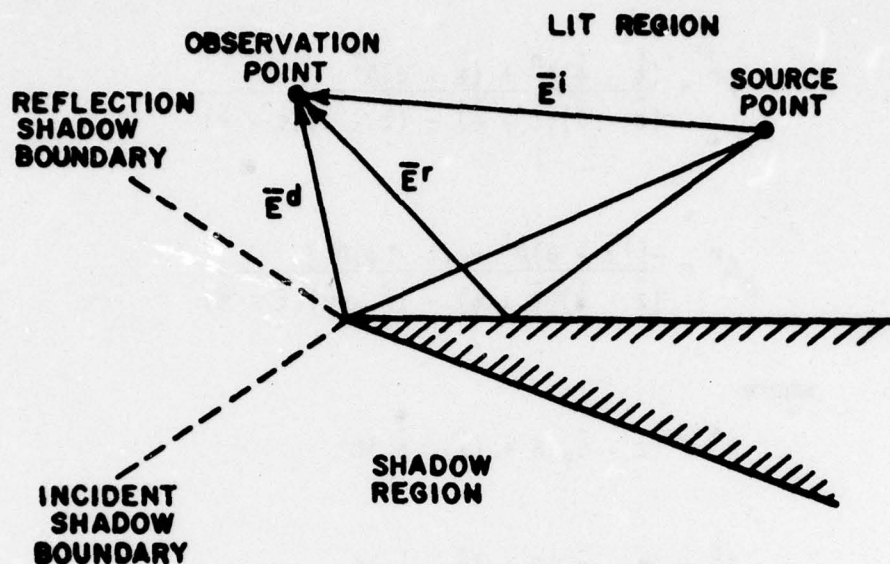INCIDENT SHADOW BOUNDARY
SHADOW REGION

Figure 3. The basic GTD wedge diffraction problem.

Kouyoumjian and Pathak [11] have derived a more rigorous basis for the GTD formulation and have shown that the diffracted field may be written compactly if placed in terms of a ray fixed coordinate system. This ray fixed coordinate system is centered at the point of diffraction Q', (or points of diffraction as in the case of plane wave incidence). Q' is a unique point or set of points for a given source and observation point. The incident ray diffracts as a cone of rays such that the cone half angle (β_0) equals the angle (β_0') which the incident ray forms with the edge as shown in Figure 4.

The orthogonal unit vectors associated with these coordinates $(\hat{s}',\hat{\beta}_0',\hat{\phi}',\hat{s},\hat{\beta}_0,\hat{\phi})$ are related by

$$\hat{I} = -\hat{s}$$

$$\hat{I} = \hat{\beta}_0' \times \hat{\phi}'$$

$$\hat{s} = \hat{\beta}_0 \times \hat{\phi}$$

where $\hat{I}$ is the incident direction unit vector and $\hat{s}$ is the unit vector in the direction of diffraction.
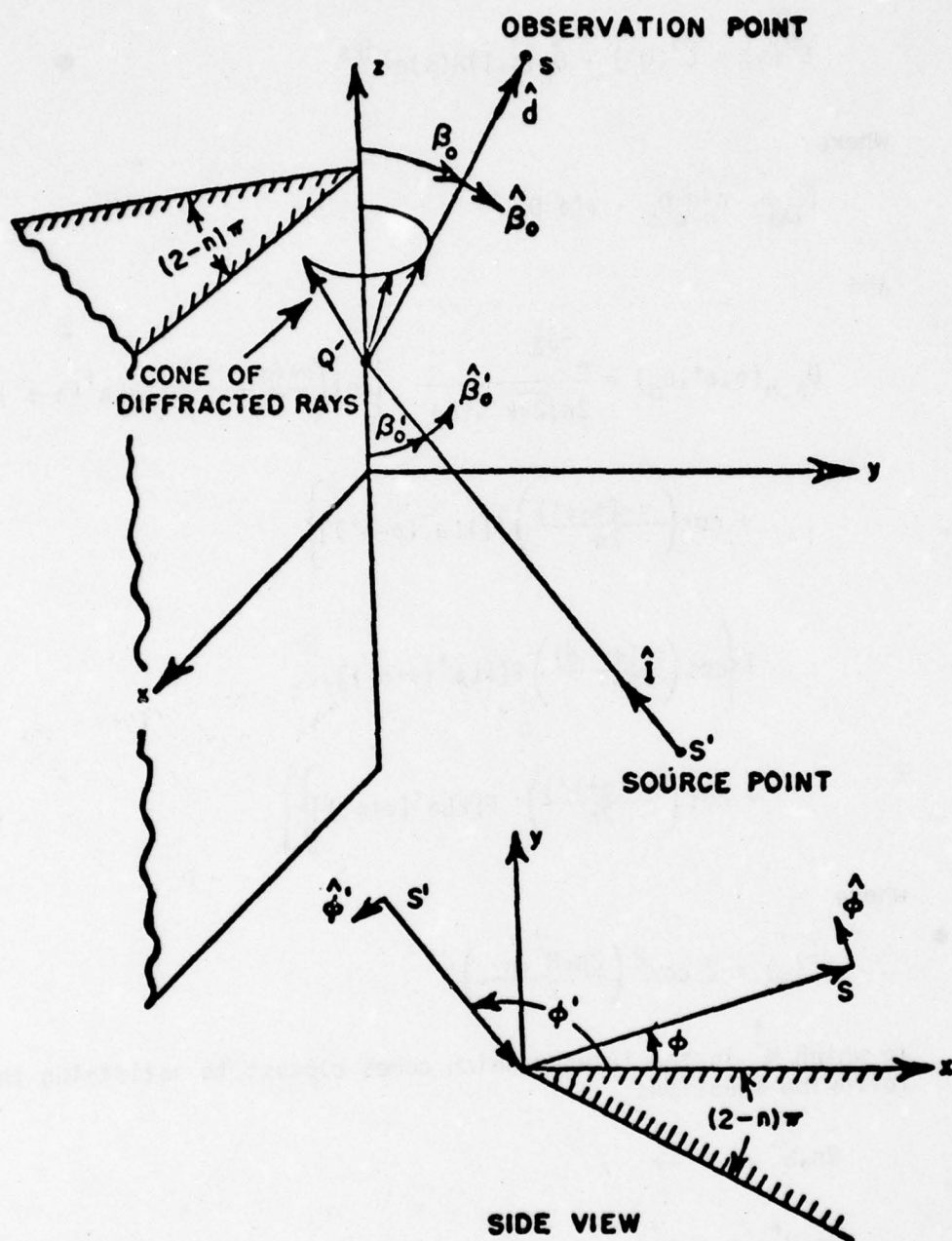
6

Figure 4. Geometry for three-dimensional wedge diffraction problem.

7

The diffracted field is then given by

$$\vec{E}^d(s) \sim \vec{E}^i(Q') \cdot \overline{\overline{D}}_E(\hat{s},\hat{I})A(s)e^{-jks}$$

where

$$\overline{\overline{D}}_E = -\hat{\beta}_0'\hat{\beta}_0 D_s - \hat{\phi}'\hat{\phi} \, D_h$$

and

$$D_{s,h}(\phi,\phi',\beta_0) = \frac{e^{-j\frac{\pi}{4}}}{2n\sqrt{2\pi k}\,\sin\beta_0} \left[\left\{ \cot\left(\frac{\pi+(\phi-\phi')}{2\pi}\right) F[kLa^+(\phi-\phi')] \right. \right.$$

$$+ \cot\left(\frac{\pi-(\phi-\phi')}{2n}\right) F[kLa^-(\phi-\phi')] \right\}$$

$$\mp \left\{ \cot\left(\frac{\pi+(\phi+\phi')}{2n}\right) F[kLa^+(\phi+\phi')] \right.$$

$$\left. \left. + \cot\left(\frac{\pi-(\phi+\phi')}{2n}\right) \, F[kLa^-(\phi+\phi')] \right\} \right] \tag{5}$$

where

$$a^{+}_{-}(\beta) = 2\cos^2\left(\frac{2n_\pi N^{+}_{-}-\beta}{2}\right)$$

in which N^{+}_{-} is the integer which comes closest to satisfying the following equations

$$2n_\pi N^- - \beta = -\pi$$

$$2n_\pi N^+ - \beta = +\pi$$

with $\beta = \phi \pm \phi'$. $F(x)$ is defined by

8

$$F(x) = 2j|\sqrt{x}| \, e^{jx} \int_{|\sqrt{x}|}^{\infty} e^{-j\tau^2} \, d\tau$$

and is called the transition function. The quantity n is defined by the wedge angle WA where WA = $(2-n)\pi$. For the elliptic disk case n = 2. The $\phi-\phi'$ terms are associated with the incident field; whereas, the $\phi+\phi'$ terms are associated with the reflected field. The quantities A(s) and L are defined later.

In matrix notation the diffracted field is expressed by [9,10]

$$\begin{bmatrix} E_{\parallel}^{d}(s) \\ E_{\perp}^{d}(s) \end{bmatrix} = \begin{bmatrix} -D_s & 0 \\ 0 & -D_h \end{bmatrix} \begin{bmatrix} E_{\parallel}^{i}(Q') \\ E_{\perp}^{i}(Q') \end{bmatrix} A(s)e^{-jks} . \qquad (6)$$

The D_s coefficient corresponds to the $\vec{E}$-field component parallel to the edge with the boundary condition (acoustically soft) or

$$(\vec{E}|_{wedge}) = 0.$$

The D_h coefficient corresponds to the $\vec{E}$-field component perpendicular to the edge with the boundary (acoustically hard) or

$$\left(\frac{\partial \vec{E}}{\partial \hat{n}} \bigg|_{wedge}\right) = 0.$$

The quantity A(s) in Equation (6) is a ray divergent factor given in general by [12]

$$A(s) = \sqrt{\frac{\rho}{s(\rho+s)}} \quad .$$

For the wedge case $\rho=\rho_e^{i}$ which is the radius of curvature of the incident wavefront in the plane containing the incident ray and the edge. For spherical wave incidence A(s) is given by

$$A(s) = \sqrt{\frac{s'}{s(s' + s)}} \quad .$$

9

The quantity L is a distance parameter and is given in general by [12]

$$L = \frac{s(\rho_e + s)\rho_1 \rho_2 \sin^2 \beta_0}{\rho_e(\rho_1 + s)(\rho_2 + s)}$$

where ρ_1 and ρ_2 are the principal radii of curvature of the wavefront. For a straight edge, L is given by [12]

$$L = \frac{s's \sin^2 \beta_0}{s + s'} \tag{7}$$

for spherical wave incidence.

At grazing incidence ($\phi' = 0$) D_s and D_h must be halved since the incident and reflected fields merge together and only half of the total field on the surface is the incident field with the other half being the reflected field.

CHAPTER III
SCATTERING FROM AN ELLIPTIC DISK USING THE
GEOMETRICAL THEORY OF DIFFRACTION

A.   INTRODUCTION

The scattering by an elliptic disk is analyzed in this chapter using the Geometrical Theory of Diffraction discussed in Chapter II. The geometry of the disk is illustrated in Figure 1 with the source located in the near zone of the disk, and the far zone scattered fields are computed.

B.   INCIDENT FIELD

The incident field from the source is given using Equation (1) by

$$\vec{E}^i(\theta,\phi) = [\hat{\theta}F(\theta,\phi) + \hat{\phi}G((\theta,\phi)] \, \frac{e^{-jks}}{s} \qquad (8)$$

where $s = d + \vec{x}_s \cdot \hat{d}.$

The vector $\hat{d}$ is the far field observation direction given by

$$\hat{d} = \cos \phi \, \sin \theta \, \hat{x} + \sin \phi \, \sin \theta \, \hat{y} + \cos \theta \, \hat{z}$$

and d is the distance from the origin to the far field observer with $\vec{x}_s$ as the source location as in Figure 5. The phase is referred to the origin using the usual far field approximation yielding

$$\frac{e^{-jks}}{s} \sim \frac{e^{-jkd}}{d} \, e^{-jk\vec{x}_s \cdot \hat{d}} \, .$$

It is possible for the source to radiate in all directions provided that the ray path from the source to the observation point is not blocked by the elliptic disk. If the source ray is blocked, then the source field in that direction is set equal to zero since the disk is assumed to be perfectly conducting.
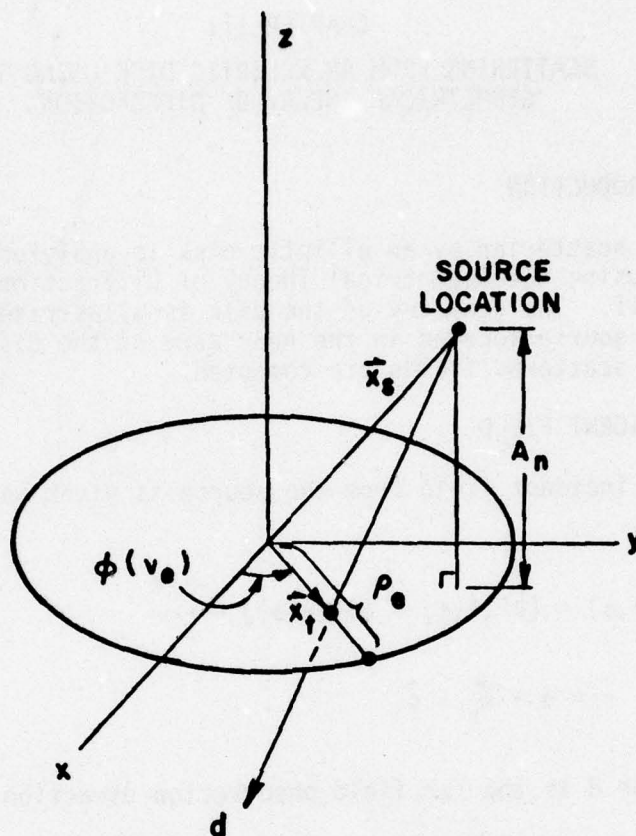
Figure 5.   Intersection of incident ray
with elliptic disk.

The first test implemented to determine if the observation direction vector ($\vec{d}$) and the vector ($\vec{x}_s$) from the center of the ellipse to the source are on opposite sides of the elliptic disk as in Figure 5. This is accomplished by comparing the sign of $\hat{z} \cdot \vec{x}_s$ and $\hat{z} \cdot \hat{d}$. If the sign of these two dot products is the same, then no shadowing can occur in that the source and the observer are on the same side of the elliptic disk. If the sign is opposite, further testing is needed.

For the next test, the intersection of the incident ray and the plane of the ellipse is found by

$$\vec{x}_t = \vec{x}_s - \frac{A_n}{D_n} \hat{d}$$

12

where A_n is the orthogonal distance from the source to the plane of the ellipse ($A_n = \vec{x}_s \cdot \hat{z}$) and D_n is the projection of $\hat{d}$ onto $\hat{z}$ ($D_n = \hat{d} \cdot \hat{z}$).

The shadowing test is then defined such that if $|\vec{x}_t| > \max(a,b)$ then the source is not shadowed. If $|\vec{x}_t| < \min(a,b)$ shadowing will occur. If $\min(a,b) < |\vec{x}_t| < \max(a,b)$ a final test is implemented which compares $|\vec{x}_t|$ with the exact distance from the center of the ellipse to the edge as depicted in Figure 5. The angular elliptic parameter in the desired direction is found using

$$v_e = \tan^{-1} \frac{a \, \vec{v}_t \cdot \hat{y}}{b \, \vec{v}_t \cdot \hat{x}} \quad .$$

The radial distance from the center of the ellipse to the elliptic edge in this direction is found from

$$\rho_e = \sqrt{a^2 \cos^2 v_e + b^2 \sin^2 v_e} \quad .$$

Finally, if $\rho_e < |\vec{x}_t|$ no shadowing will occur and if $\rho_e \geq |\vec{x}_t|$, the incident ray is shadowed.

C. REFLECTED FIELD

Reflections off the elliptic disk are possible only if the observation point and the source are located on the same side of the disk. This is equivalent to saying that the observation direction ($\hat{d}$) and the vector ($\vec{x}_i$) from the center of the ellipse to the image location are on opposite sides of the elliptic disk as in Figure 2. The image location is given by

$$\vec{x}_i = \vec{x}_s - 2 A_n \hat{z}$$

where $A_n = \vec{x}_s \cdot \hat{z}$.

The procedure, used to determine if a reflected field exists, parallels the section on source shadowing by the ellipse except for some minor changes. The reflected field exists only if the ray from the image source in the scatter direction ($\hat{d}$) intersects the elliptic disk. If this intersection does not occur the reflected field is set equal to zero.

If it is determined that a reflected field exists, then the reflected field is expressed by

13

$$\vec{E}^r(\theta,\phi) = [\hat{\theta}F^r(\theta,\phi) + \hat{\phi}G^r(\theta,\phi)] \frac{e^{-jkd}}{d} e^{-jk\vec{X}_i \cdot \hat{d}}$$

and $F^r(\theta,\phi)$ and $G^r(\theta,\phi)$ can be found using Equations (4a) and (4b). The angles of incidence θ_i and ϕ_i from the source to the point of reflection are found by defining

$$\vec{I} = \frac{A_n}{D_n} \hat{d} - z A_n \hat{z} = I_x\hat{x} + I_y\hat{y} + I_z\hat{z}$$

which is the vector from the source to the point of reflection located at $\vec{X}_i + A_n/D_n$ $\hat{d}$ where $D_n = \hat{d} \cdot \hat{z}$. θ_i and ϕ_i are then found by solving

$$\theta_i = \tan^{-1}\left(\frac{\sqrt{I_x^2 + I_y^2}}{I_z}\right)$$

$$\phi_i = \tan^{-1}\left(\frac{I_y}{I_x}\right) .$$

D. DIFFRACTED FIELD

The diffracted field from an elliptic disk is normally generated from discrete points along the elliptic rim which satisfy the law of diffraction. This law states that at the diffraction point (Q'), the angle of incidence and the diffracted cone half-angle are equal. This law is expressed in the geometry of Figure 6 as

$$\cos \beta_0' = \cos \beta_0$$

or

$$\hat{I}(v) \cdot \hat{e}(v) = \hat{d} \cdot \hat{e}(v) \tag{9}$$

where $I(v)$ is the unit vector from the source to the diffraction point (Q'). If Q' is located at the point $(a \cos v\ \hat{x} + b \sin v\ \hat{y})$ and the source is located at $\vec{X}_s = x_s\hat{x} + y_s\hat{y} + z_s\hat{z}$ then
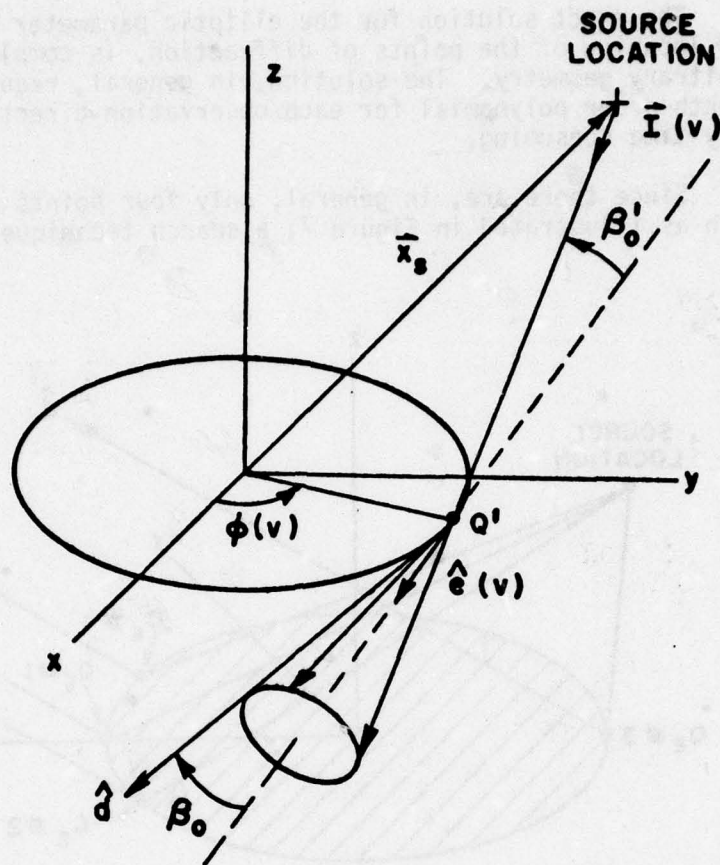
14

Figure 6. Diffracted field geometry.

$$\hat{I}(v) = \frac{(a \cos v - x_s)\hat{x} + (b \sin v - y_s)\hat{y}}{\sqrt{(a \cos v - x_s)^2 + (b \sin v - y_s)^2}} \ .$$

The quantity $\hat{e}(v)$ is the unit vector tangent to the edge at Q' and is given by

$$\hat{e}(v) = \frac{-a \sin v \ \hat{x} + b \cos v \ \hat{y}}{\sqrt{a^2 \sin^2 v + b^2 \cos^2 v}} \ .$$

15

The exact solution for the elliptic parameter v, which specifies the location of the points of diffraction, is complicated for an arbitrary geometry. The solution, in general, requires solving an eighth-order polynomial for each observation direction which becomes very time consuming.

Since there are, in general, only four points of diffraction such as illustrated in Figure 7, a search technique has been used to
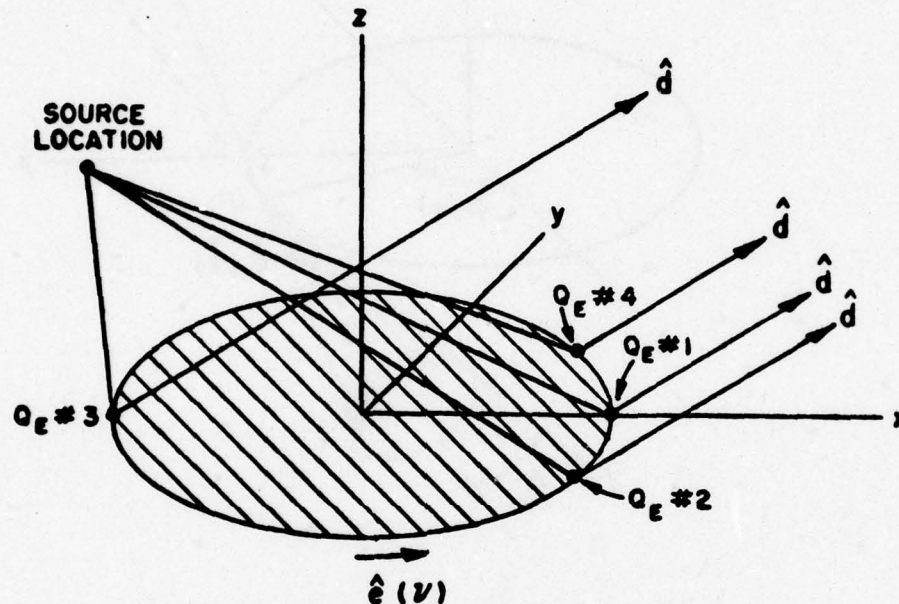

Figure 7. Curved wedge diffraction points on rim of elliptic disk.

find these points of diffraction along the elliptic rim. The method is based upon the minimization of the difference between the two dot products given in Equation (9). An error term is given by

$$\varepsilon(v) = \hat{I}(v) \cdot \hat{e}(v) - \hat{d} \cdot \hat{e}(v).$$

The minimum error is found by first forming

$$\xi_j = \varepsilon(v_{j-1}) + \varepsilon(v_j) + \varepsilon(v_{j+1}) \quad \text{for } j = 0 \text{ to } 360. \quad \text{If}$$

$|\xi_j| \leq |\xi_{j-1}|$ and $|\xi_j| \leq |\xi_{j+1}|$, then v_j is the closest degree to a minimum in the error. In order for this minimum to be a diffraction

16

point, the error term must reduce to zero. This technique, however, will also find a minimum in the error which is not a zero crossing. In order to remove this problem and to determine the point of diffraction closer than one degree increments, an interpolation scheme is used which is given by

$$v_{diff} = v_j + \Delta v$$

where Δv is defined as

$$\Delta v = \frac{|\vec{T}| \ (\vec{e} \cdot \hat{d}) - (\vec{e} \cdot \hat{I})}{|\vec{e}| + \Delta\vec{e} \cdot \vec{T} - |\vec{T}| \ (\Delta\vec{e} \cdot \hat{d}) - (\vec{e} \cdot \hat{I}) \ (\vec{e} \cdot \hat{d})}$$

and

$$\Delta\vec{e} = \frac{\partial \vec{e}}{\partial v} = -a \cos v \ \hat{x} - b \sin v \ \hat{z}.$$

If $|\Delta v| > 1$ then the point found is not a diffraction point but a minimum in the error function and is ignored.

The location of these diffraction points on the rim of the elliptic disk depends upon the source location, the observation direction, and the physical dimensions of the ellipse. If the source is located on the z-axis through the center of the ellipse, as in Figure 8, the only physical dimensions necessary to locate
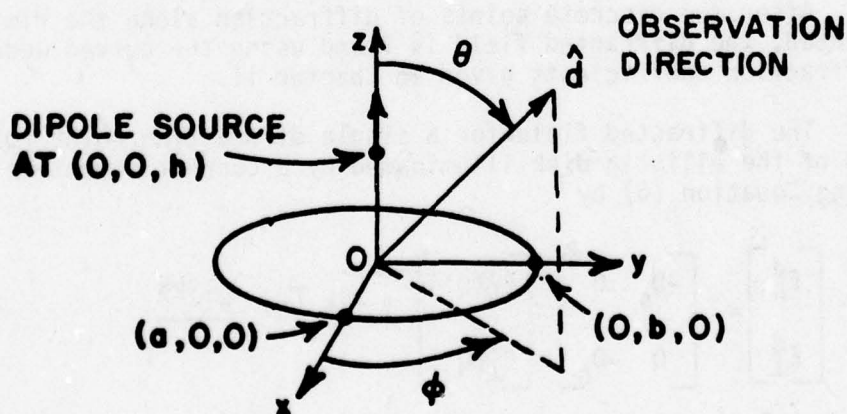

Figure 8. Dipole off an elliptic disc.

17

the diffraction points are the axial ratio and the height ratio. The axial ratio is defined as the ratio a/b. The height ratio is defined as the ratio h/b. The quantities a, b, and h are illustrated in Figure 8.

The location of the diffraction points on an ellipse with axial ratio of 0.4 and height ratio of zero for a pattern cut in the θ = 90° plane (refer to Figure 8) are shown in Figure 9a. In Figure 9b four observation directions were chosen from Figure 9a to demonstrate where the points of diffraction occur. For example at ϕ = 25° four diffraction points occur at v = 10.5°, 135.6°, 161.0, and 233.9° which are labeled 5, 6, 7 and 8, respectively on both figures.

The location of the points of diffraction as a function of increasing height ratio, i.e., as the antenna is moved off the disk along the z-axis, is illustrated in Figure 10. The pattern cut for this case is in the ϕ= 90° plane for an ellipse with an axial ratio of 0.4.

It is shown in Figure 11 how the location of these diffraction points are effected as the observation direction is scanned from the ϕ = 90° plane to the ϕ = 180° plane in 10° increments. For this case the axial ratio is 0.4 and the source is in the center of the disk (height ratio is zero). Note that in these figures if θ and ϕ are defined, then either two or four diffraction points exist.

The effect of changing the axial ratio is shown in Figure 12 for an ellipse with the source in the center of the disk and the pattern taken in the ϕ = 90° plane.

After the discrete points of diffraction along the rim have been located, the diffracted field is found using the curved wedge diffraction coefficients given in Chapter II.

The diffracted field for a single diffraction point (Q') on the rim of the elliptic disk illuminated by a current moment is given using Equation (6) by

$$
\begin{bmatrix} E_{\parallel}^d \\ \\ E_{\perp}^d \end{bmatrix} = \begin{bmatrix} -D_s & 0 \\ \\ 0 & -D_h \end{bmatrix} \begin{bmatrix} E_{\parallel}^i(Q') \\ \\ E_{\perp}^i(Q') \end{bmatrix} \sqrt{\rho}\, e^{-jk\,\vec{I}\cdot\hat{d}}\; \frac{e^{-jkd}}{d} \quad .
$$

The dyadic diffraction coefficients for this case are found using Equation (5). The distance parameter L in the far field reduces to
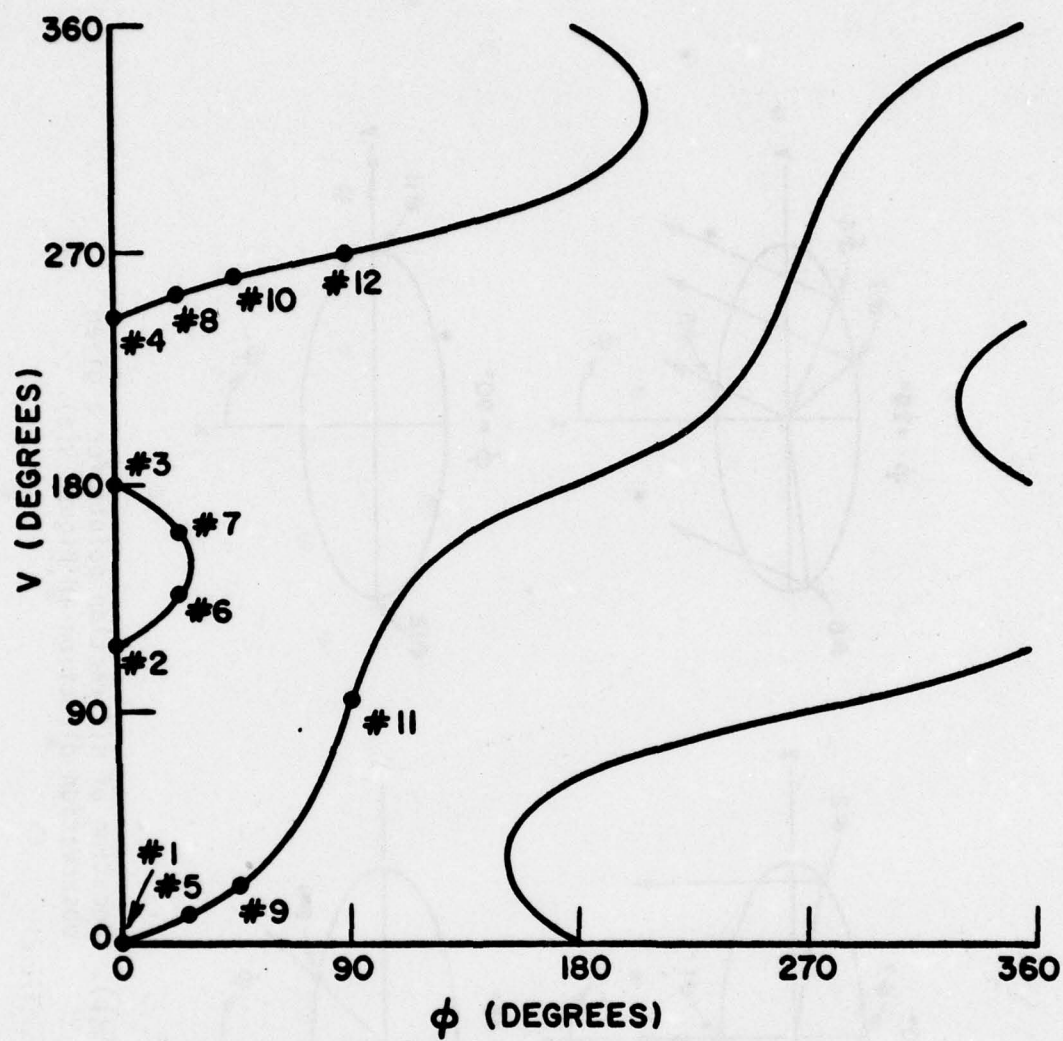
18

Figure 9(a). Location of diffraction points on an ellipse
as a function of observation angle (θ=90°,
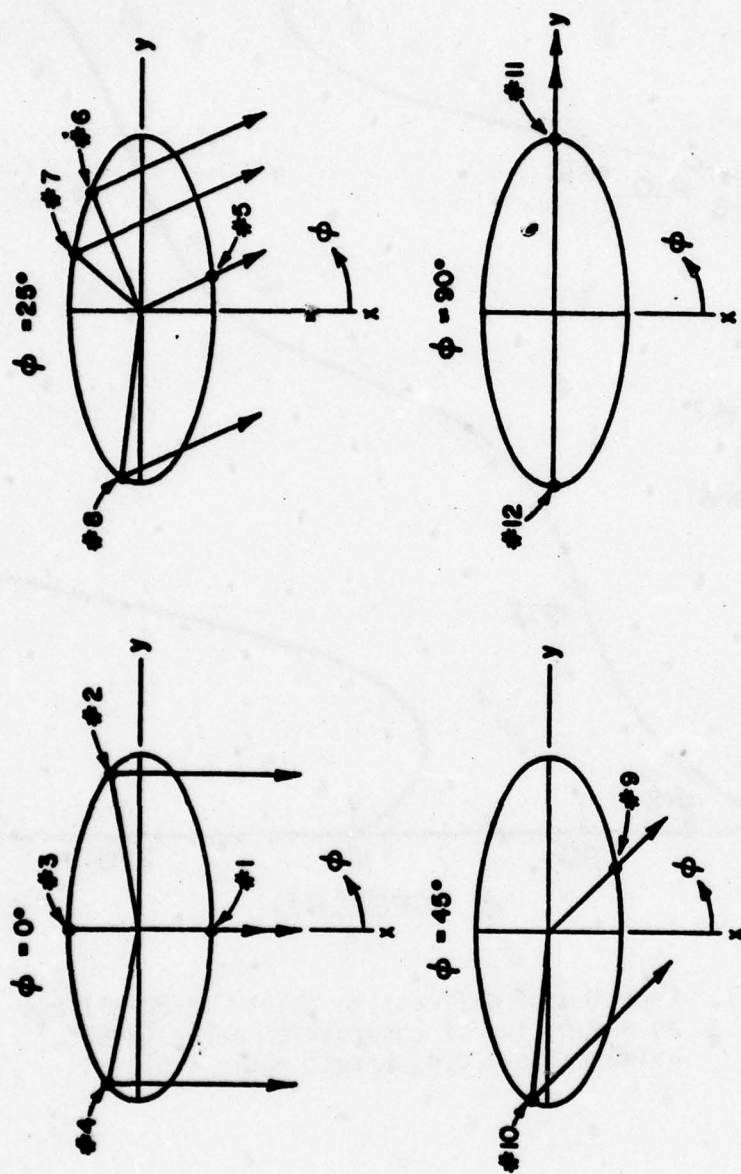axial ratio = 0.4, height ratio = 0).

19

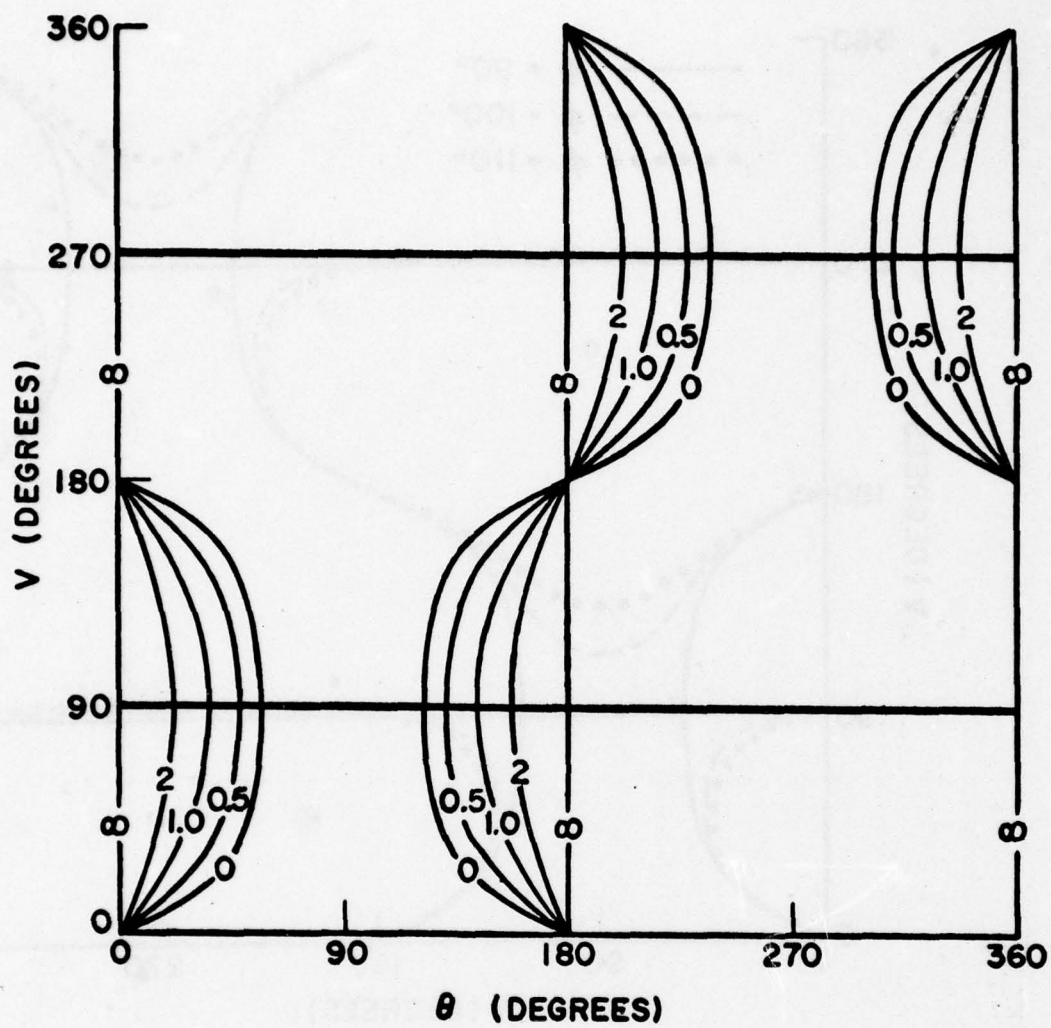Figure 9(b). Location of diffraction points for a given observation direction in Figure 9(a).

20

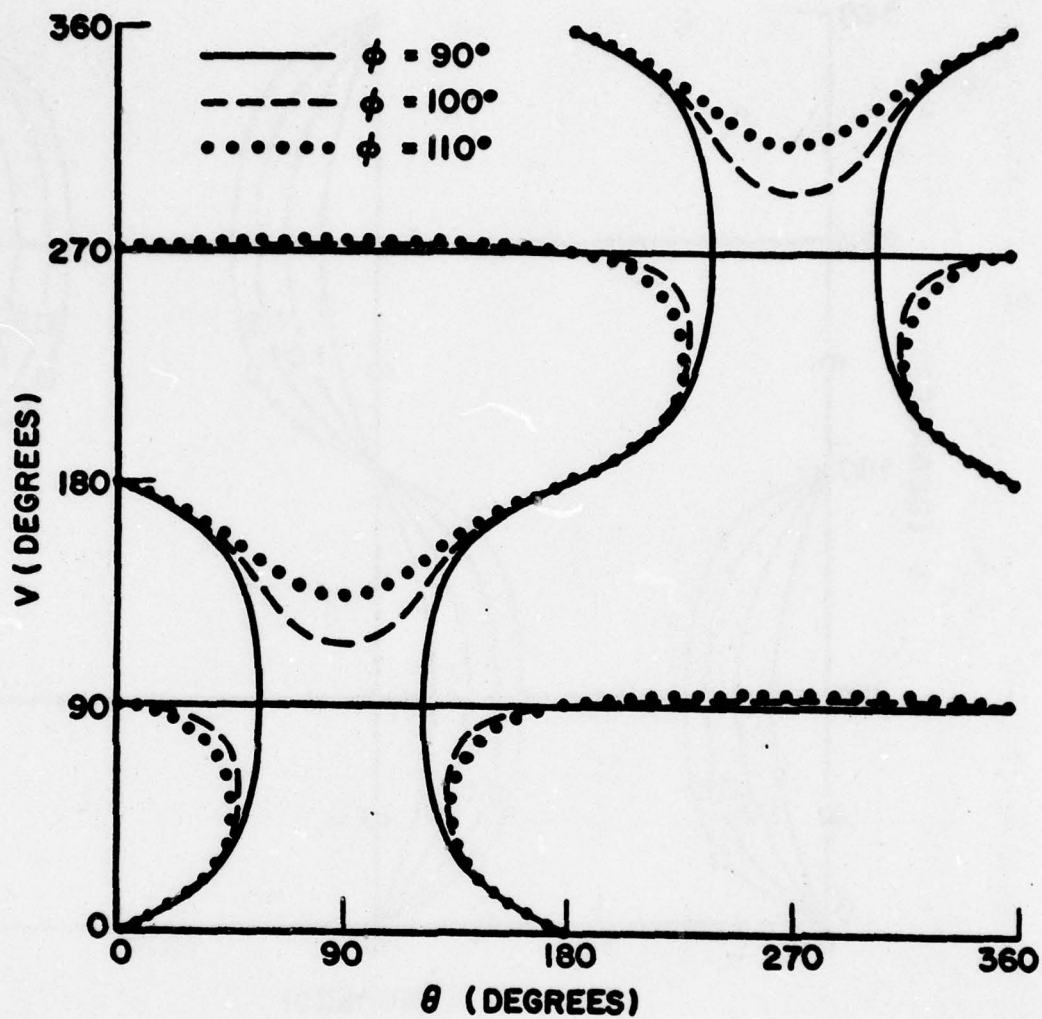Figure 10.   Location of diffraction points as a function of height ratio ($\phi=90°$, axial ratio = 0.4).

21

Figure 11(a). Location of diffraction points as a function of observation direction (ϕ=90°-110°, axial ratio = 0.4, height ratio = 0).

22
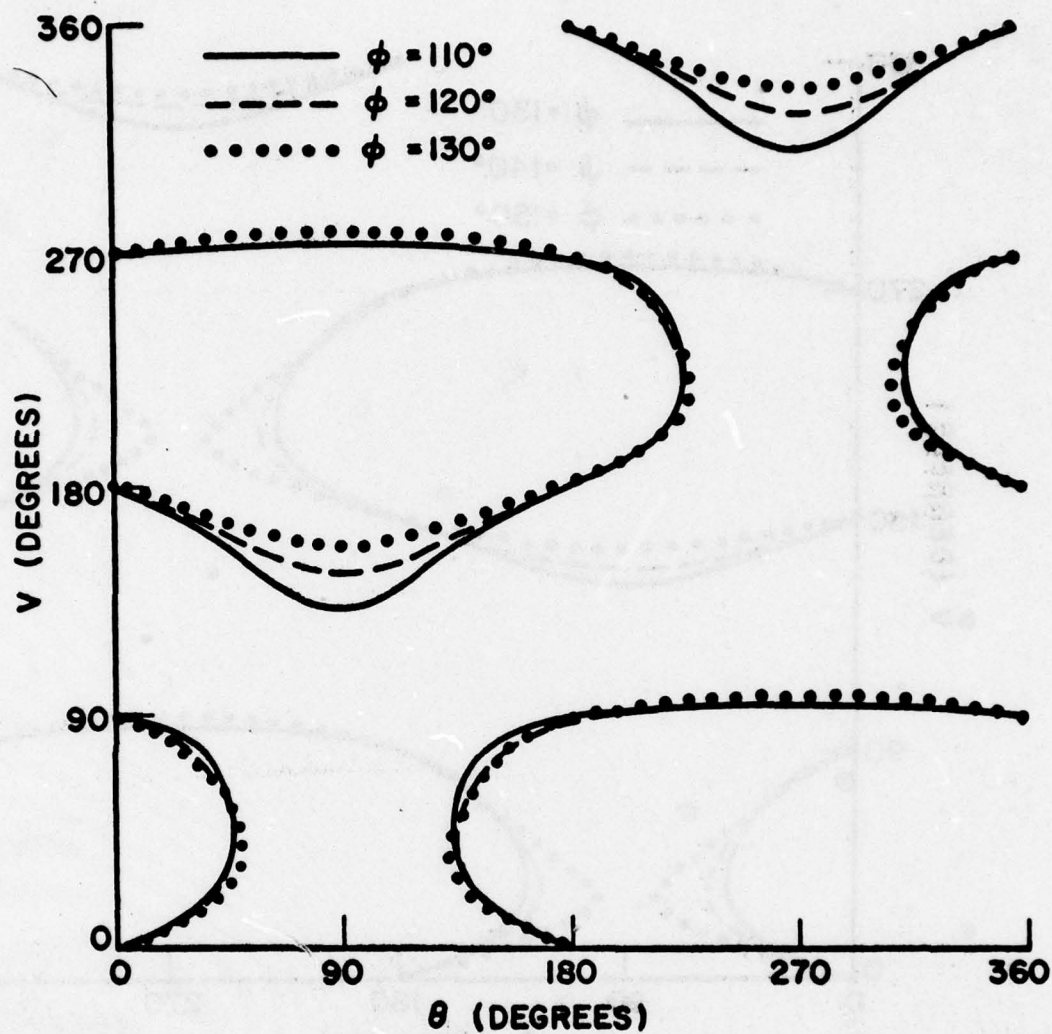
Figure 11(b). Location of diffraction points as a function of observation direction (ϕ=110°-130°, axial ratio = 0.4, height ratio = 0).
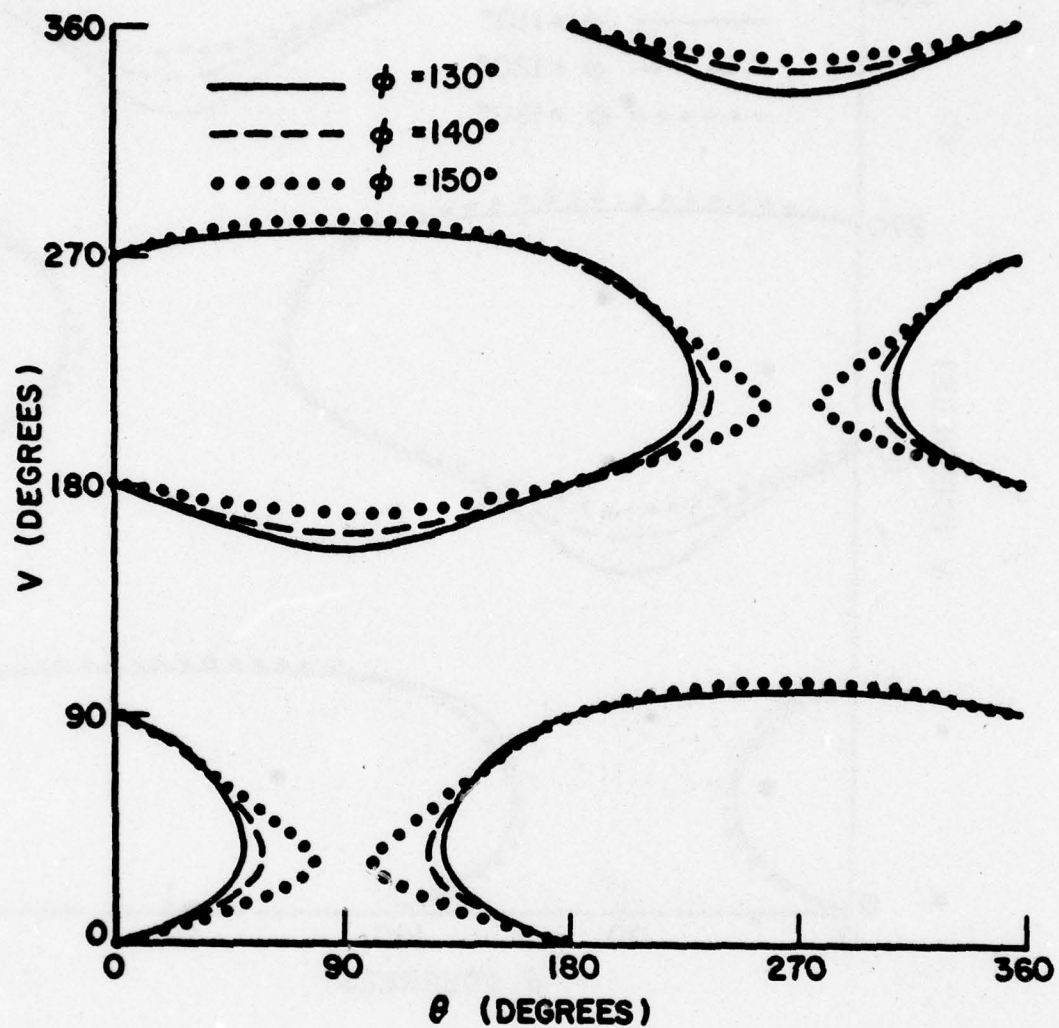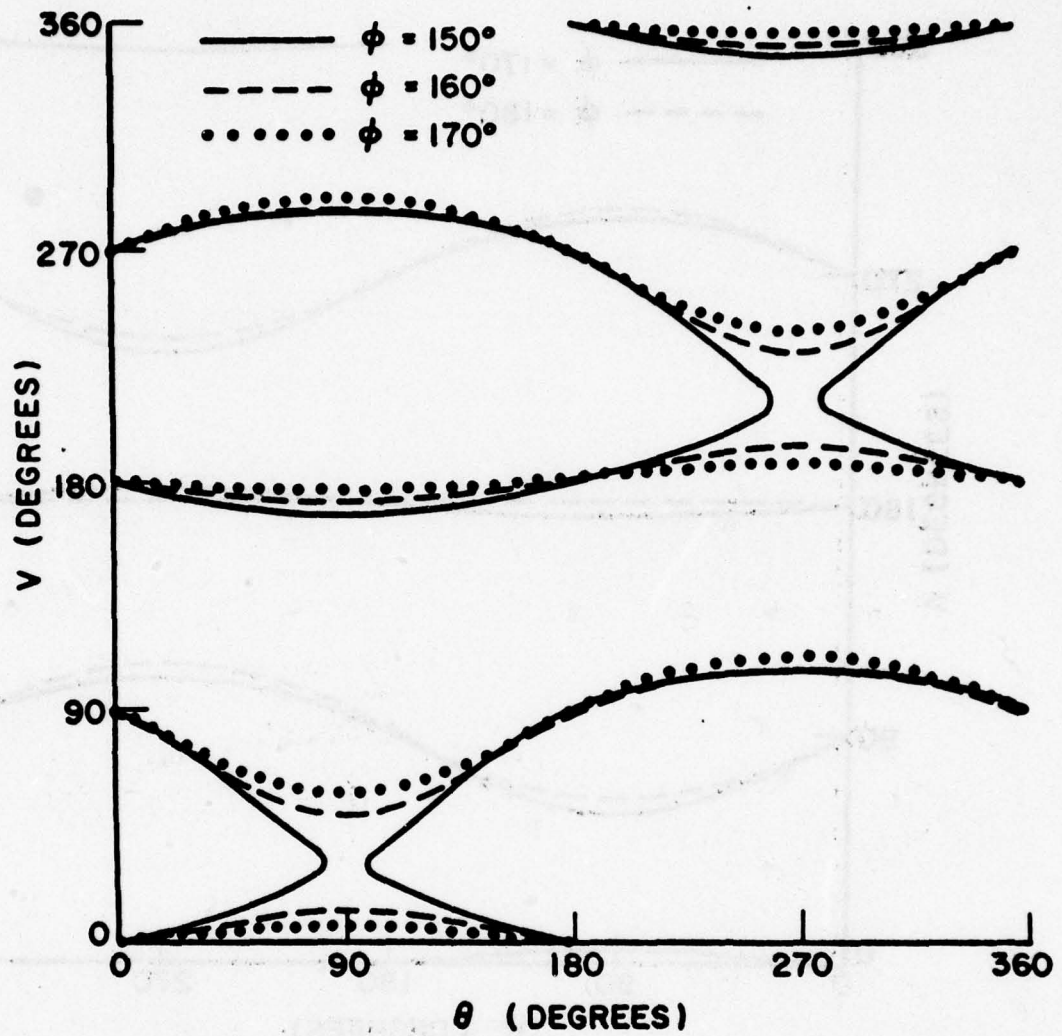
Figure 11(c). Location of diffraction points as a function of
observation direction (φ=120°-150°, axial ratio
= 0.4, height ratio = 0.

24

Figure 11(d). Location of diffraction points as a function of observation direction (ϕ=150°-170°, axial ratio = 0.4, height ratio = 0).

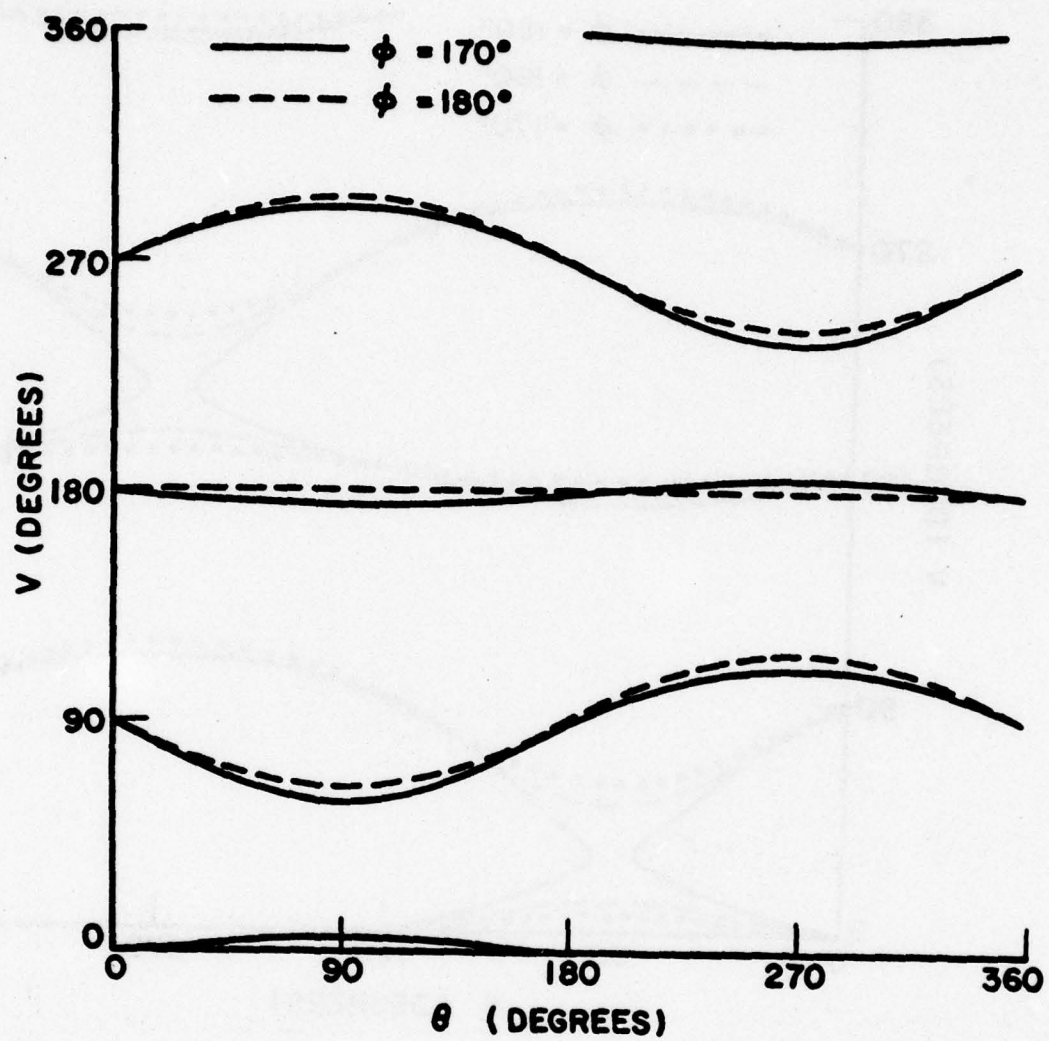Figure 11(e). Location of diffraction points as a function of observation direction (ϕ=170°-180°, axial ratio = 0.4, height ratio = 0).
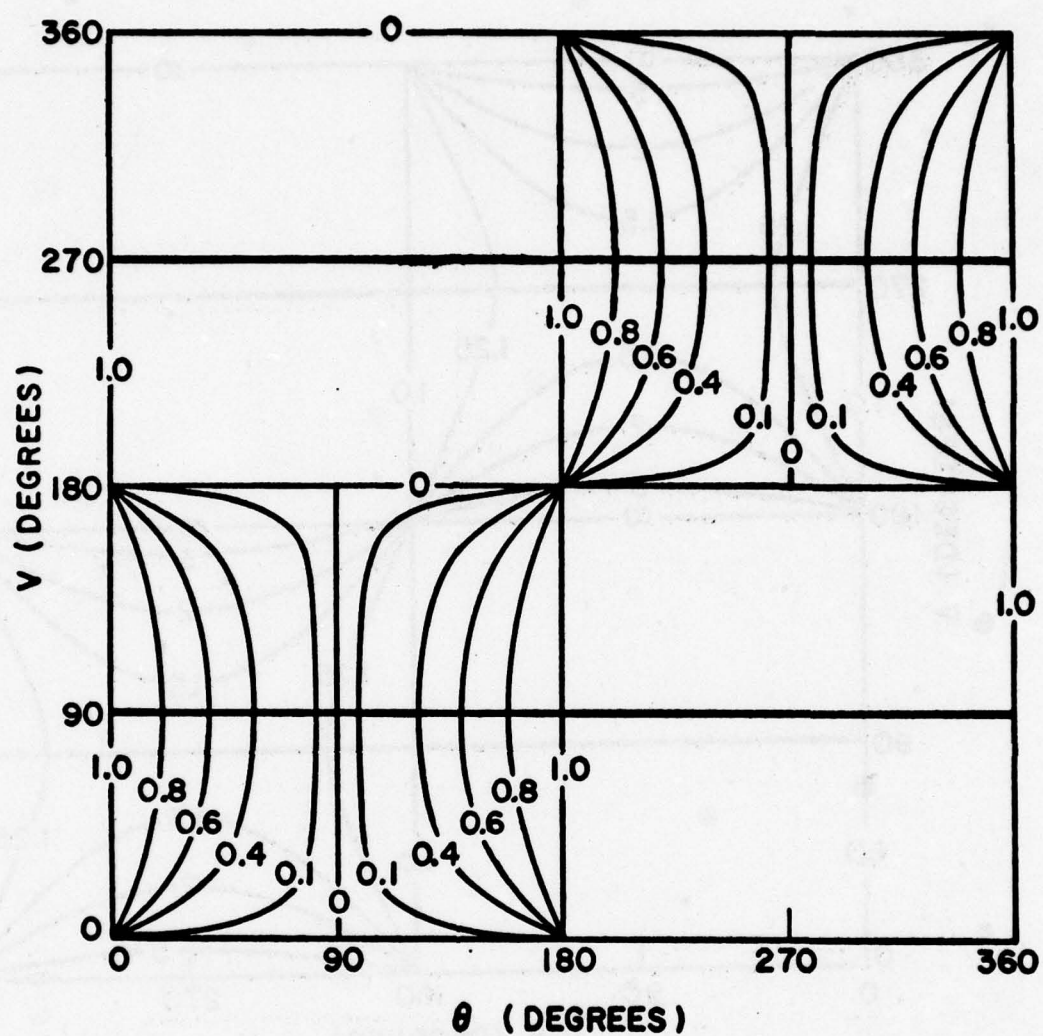
26

Figure 12(a). Location of diffraction points as a function of
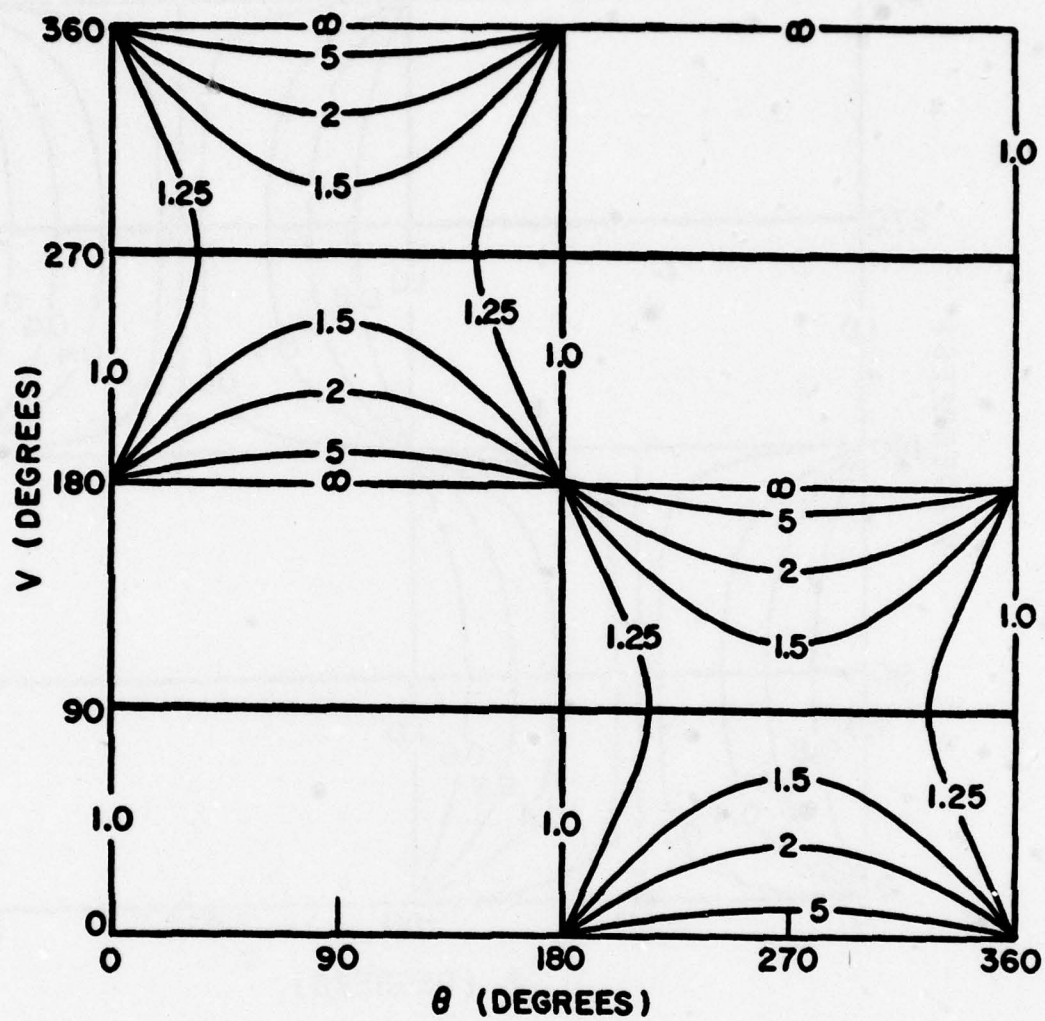axial ratio ($\phi=90°$, height ratio = 0).

27

Figure 12(b). Location of diffraction points as a function of axial ratio (ϕ=90°, height ratio = 0).

$$L = s' \sin^2 \beta_0$$

where $\quad s' = |\vec{I}|$.

The total diffracted field is obtained by summing each of the diffracted field terms provided that the points of diffraction are separated. It has been determined that if the diffraction points are separated there are a maximum of four such points which will satisfy the laws of diffraction such as shown in Figure 7. This four point diffraction solution when combined with the incident and reflected fields usually predicts patterns which are in very good agreement with experimental results. However for certain geometries and observation directions, caustics can occur.

The axial caustic occurring if the antenna is located on axis near a circular disk (see Figure 13) has been treated by Ryan and
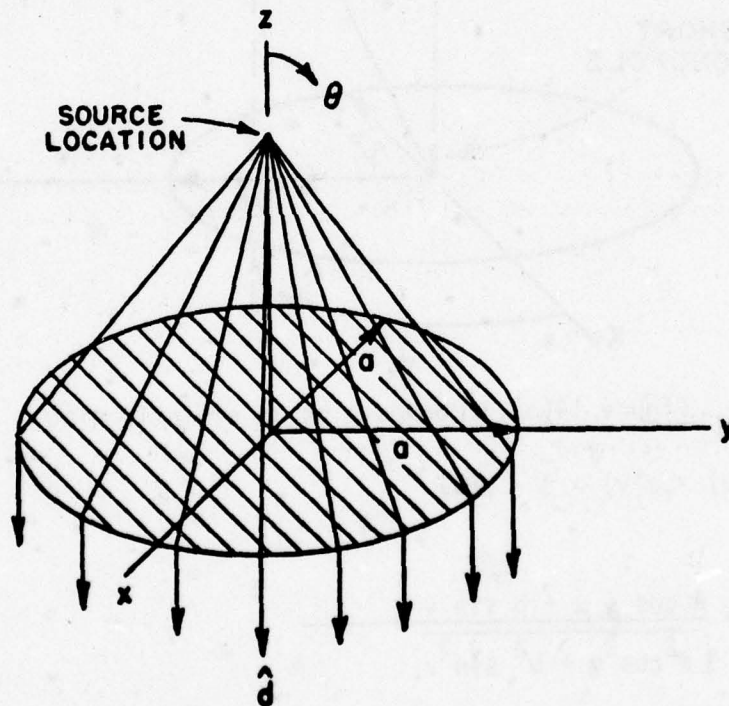

Figure 13. Axial caustics of a circular disk.

Peters [13]. With this geometry an infinite number of diffraction points exist along the rim of the disk for axial observation. directions ($\theta = 0$ or π). The infinite number of diffraction points

29

implies that an infinite field exists in the neighborhood of $\theta = 0$ or π which of course, is not the true physical result. However, the equivalent current solution given in the next section can be used to correct the diffracted fields in these caustic regions (i.e., the sectors where the diffraction solution fails).

A pseudo-caustic problem which can occur with the elliptic disk geometry is the merging of diffraction points along the rim as the observation direction is changed. This effect is illustrated using the configuration shown in Figure 14a. Solving the law of diffraction for this case yields:
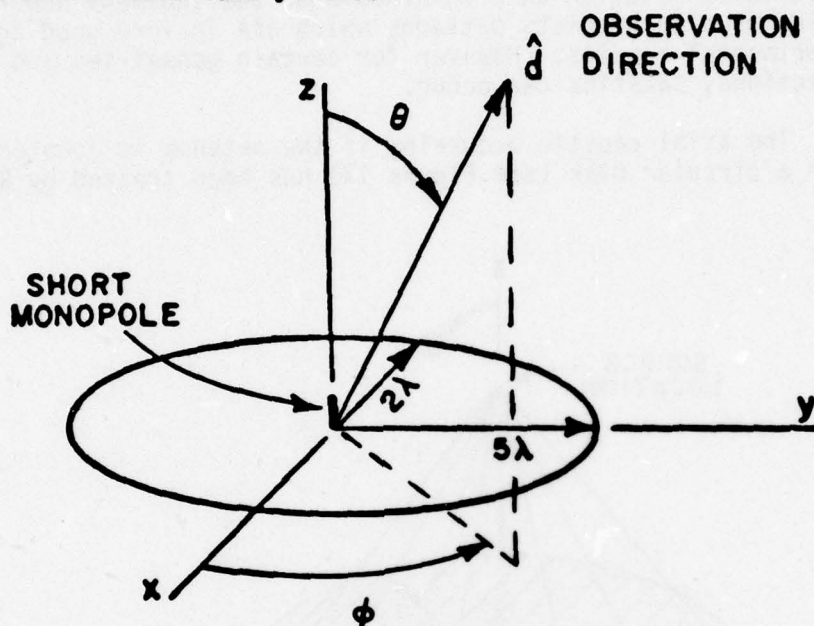

Figure 14(a). Monopole on an elliptic disc.

$$\hat{I}(v) \cdot \hat{e}(v) = \hat{d} \cdot \hat{e}(v) \tag{10}$$

where

$$\hat{I} = \frac{a \cos v \, \hat{x} + b \sin v \, \hat{y}}{\sqrt{a^2 \cos^2 v + b^2 \sin^2 v}}$$

$$\hat{e} = \frac{-a \sin v \hat{x} + b \cos v \hat{y}}{\sqrt{a^2 \sin^2 v + b^2 \cos^2 v}}$$

$$\hat{d} = \sin \theta \, \hat{x} + \cos \theta \, \hat{z}$$

with the pattern taken in the y-z plane ($\phi = 90°$).

30

Equation (10) can be reduced to give

$$b \cos v \sin \theta = \frac{(b^2-a^2)\sin v \cos v}{\sqrt{a^2\cos^2 v + b^2\sin^2 v}} \quad . \tag{11}$$

If $\cos v = 0$, the equality holds; therefore, $v = \pm \pi/2$ are two diffraction points. If $\cos v \neq 0$ then the possibility of two other diffraction points exists and Equation (11) becomes

$$b \sin \theta = \frac{(b^2-a^2)\sin v}{\sqrt{a^2\cos^2 v + b^2 \sin^2 v}} \quad .$$

Squaring both sides of this equation and solving for $\tan v$, leads to

$$\tan v = \pm \frac{ab \sin \theta}{\sqrt{(b^2-a^2)^2 - b^4\sin^2 \theta}} \quad .$$

The above equation has two real solutions for v if

$$(b^2-a^2)^2 > b^4 \sin^2 \theta$$

which implies

$$|\sin \theta| < \left|1 - \left(\frac{a}{b}\right)^2\right| \quad . \tag{12}$$

If the inequality is true, then four distinct diffraction points will exist. The criterion for three of the four diffraction points to merge into one occurs if $a < \sqrt{2} b$ for this pattern cut.

As an example of this pseudo-caustic effect, the case where $a = 2\lambda$ and $b = 5\lambda$ is chosen. As seen is Figure 14b caustics occur at the angles where the diffraction points merge as defined by Equation (12) or

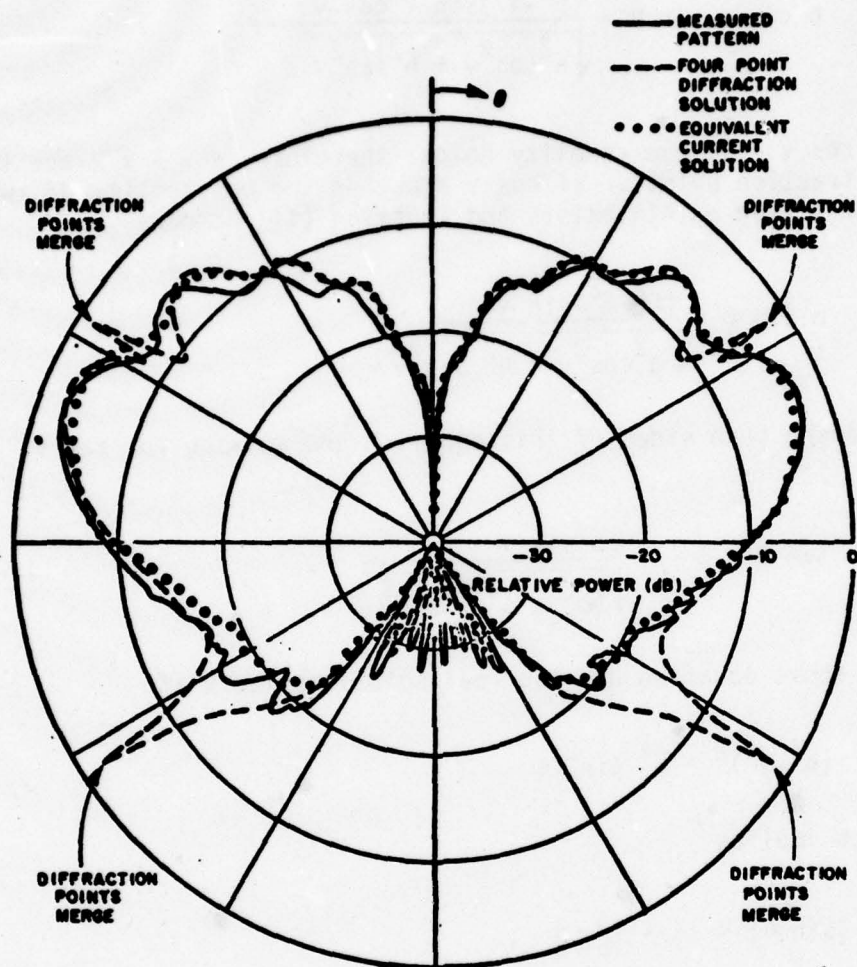$$\theta = \pm \sin^{-1} \left(1 - \left(\frac{a}{b}\right)^2\right) = \pm 57.14°, \pm 122.86°.$$

31

Figure 14(b). E-theta radiation pattern in the y-z plane
for the configuration in Figure 14(a).

The merging of these diffraction points as well as their position
along the rim is seen in Figure 15. If the pattern is taken in
the x-z plane, which is similar to letting a=5λ and b=2λ, then
a > √2 b and no caustics occur as shown in Figure 14c.
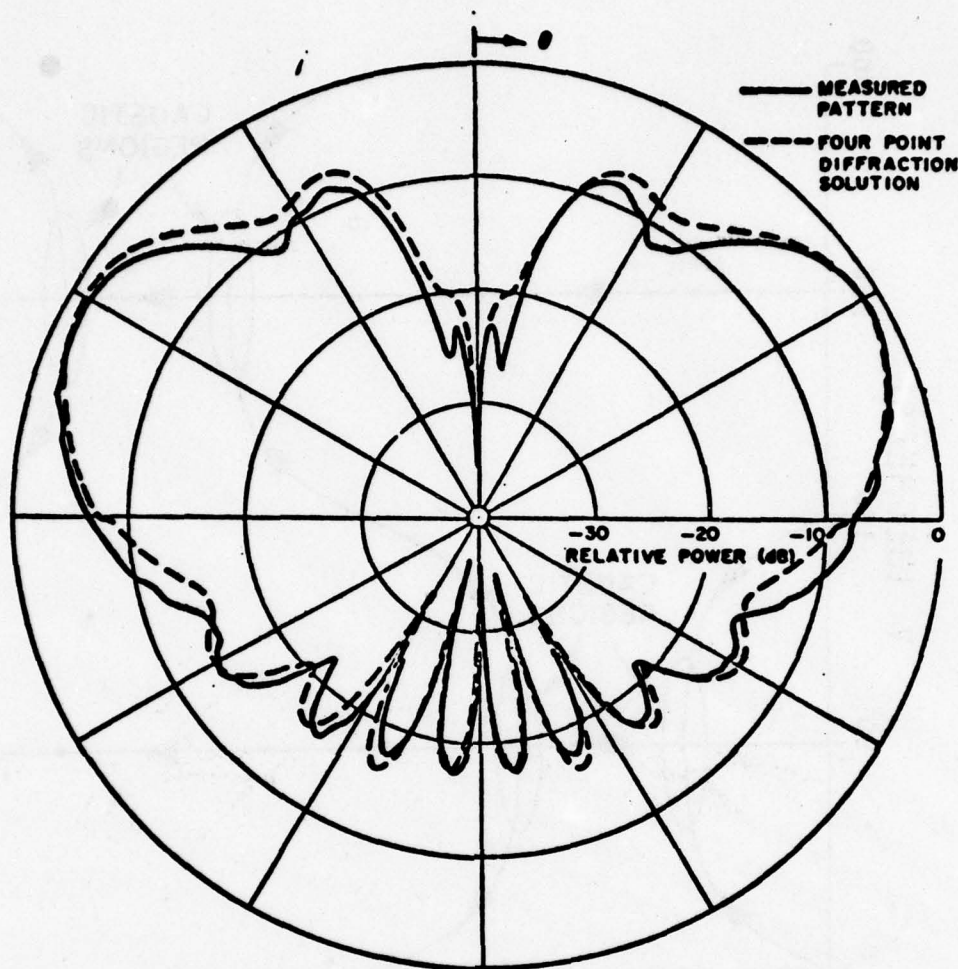
32

Figure 14(c). E-theta radiation pattern for the x-z plane
for the configuration in Figure 14(a).

The plot of the diffraction points for a given pattern cut is useful in showing where caustics can occur. As the locus of diffraction points approach a vertical line, such as in Figure 15, a caustic condition is being approached.

The use of equivalent currents as described in the next chapter can correct these pseudo-caustic effects in addition to the axial caustics discussed earlier.
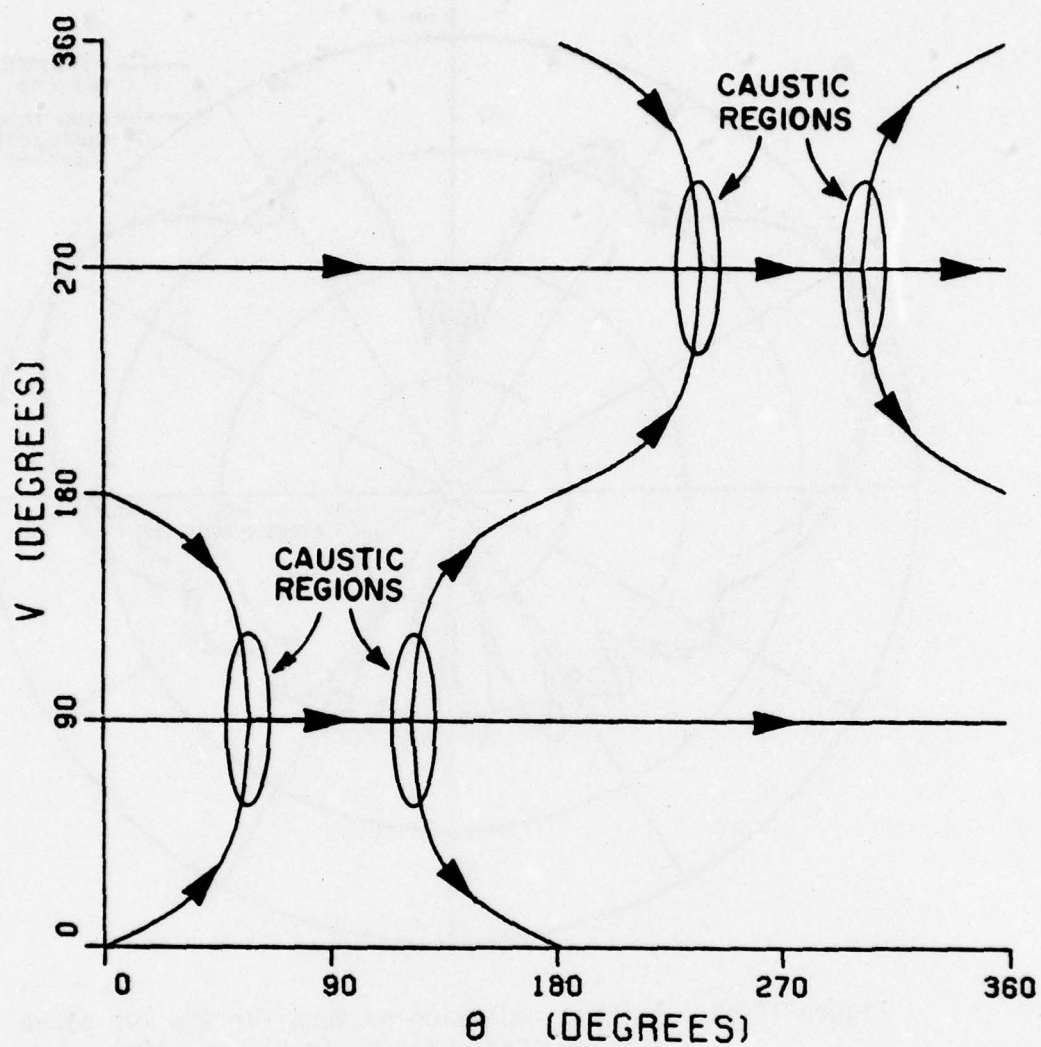
Figure 15.   Diffraction points of an ellipse as a function of
observation angle ($\phi=0°$, axial ratio = 0.4,
height ratio = 0).

34

CHAPTER IV
CAUSTIC CORRECTION VIA EQUIVALENT CURRENT

A. INTRODUCTION

The equivalent current concept was implemented by Ryan and Peters [13] to correct axial caustics occuring in the back-scattering of axially symmetric cone frustrums. This type of caustic occurs because GTD predicts infinite fields when an infinite number of diffracted rays occur. The term equivalent current is used because the currents generated are a function of the scattering direction which is not characteristic of true line currents.

The equivalent current concept is used to correct the two types of problems associated with the GTD four point diffraction solution of the previous section. The first problem is the axial type caustic similar to those dealt with by Ryan and Peters. This case occurs, for example, with a circular disk when the observation and source locations are both axially located. The second problem is a pseudo-caustic effect where GTD predicts a discontinuity in the scattering pattern whenever diffraction points merge or disappear from view. This pseudo-caustic effect can be observed on the disk when three of the four diffraction points merge into a single diffraction point or two diffraction points merge and disappear as the observation direction is changed (see Figure 15).

B. TECHNICAL APPROACH

The equivalent current method is based upon the two dimensional diffraction of a plane wave incident upon a perfectly conducting half plane. The equivalent current is found by comparing the electric and magnetic fields generated by the two dimensional diffraction process at each point along the edge with the fields which would be produced by equivalent electric and magnetic current elements. The diffracted field from the curved edge is found by numerically integrating these equivalent currents in the radiation integral.

Referring to Equation (6), the two-dimensional diffracted field at the point p is given by

$$E^d(p) = E_z^i(Q') \, D_s \, \frac{e^{-jks}}{\sqrt{s}} \tag{13a}$$

35

$$H^d(p) = H^i_z(Q') \ D_h \ \frac{e^{-jks}}{\sqrt{s}} \ . \tag{13b}$$

In terms of the equivalent electric and magnetic line currents (I_z and M_z) along the edge, these fields are

$$E^d(p) = -Z_o \ e^{j \frac{\pi}{4}} \ \sqrt{\frac{k}{8\pi s}} \ e^{-jks} \ I_z$$

$$H^d(p) = -Y_o \ e^{j \frac{\pi}{4}} \ \sqrt{\frac{k}{8\pi s}} \ e^{-jks} \ M_z.$$

Equating these two expressions implies that

$$I_z = - \frac{E^i_z(Q')}{Z_o} \ \frac{D_s(Q')}{\sin\beta_o} \sqrt{\frac{8\pi}{k}} \ e^{-j \frac{\pi}{4}} \tag{14a}$$

and

$$M_z = - \frac{H^i_z(Q')}{Z_o} \ \frac{D_h(Q')}{\sin\beta_o} \ \sqrt{\frac{8\pi}{k}} \ e^{-j\frac{\pi}{4}} \tag{14b}$$

where
$$D_s = \frac{D_s(Q',\beta_o=90°)}{\sin\beta_o} = \frac{D^*_s}{\sin\beta_o}$$

and

$$D_h = \frac{D_h(Q',\beta_o=90°)}{\sin \beta_o} = \frac{D^*_h}{\sin\beta_o} \ .$$

$E^i_z(Q')$ and $H^i_z(Q')$ are the electric and magnetic components, respectively, of the incident field parallel to the edge.

36

Using the above equivalent currents, one can show that the diffracted field for an infinite straight edge can be reproduced. This is done using the following line integrals:

$$E_\theta^d = \frac{jkz_o}{4\pi} \int I(z') \sin\theta \, (z') \frac{e^{-jks}}{s} \, dz'$$

$$E_\theta^d = -\frac{jkz_o}{4\pi} \frac{e^{-j\frac{\pi}{4}}}{z_o} \sqrt{\frac{8\pi}{k}} \int E_z^i(z') \frac{D_s^*(z')}{\sin\beta_o} \frac{\sin\theta(z')}{s} e^{-jks} dz'$$

$$E_\theta^d = e^{j\frac{3\pi}{4}} \sqrt{\frac{k}{2\pi}} \int E_z^i(z') \, D_s^*(z') \frac{\sin\theta(z')}{\sin\beta_o} \frac{e^{-jks}}{s} \, dz'. \qquad (15)$$

The above integral can be solved using a stationary phase argument since a stationary phase point occurs in the integrand of Equation (15) at the diffraction point. From stationary phase [14],

$$\int F(z') e^{-jkf(z')} dz' \cong F(z_s') \sqrt{\frac{2\pi}{k|f''(z_s')|}} \, e^{-jkf(z_s')} \, e^{-j\frac{\pi}{4} \text{sign } f''(z_s')}$$

where

$$f(z') = s + z' \cos\beta_o$$

$$f'(z') = -\cos\theta(z_s') + \cos\beta_o = 0$$

$$\theta(z') = \beta_o$$

$$f''(z') = \frac{\sin^2\beta_o}{s} > 0 \, .$$

In this case,

$$F(z') = E_z^i(z') \, D_s^*(z') \, \frac{\sin\theta \, (z')}{\sin\beta_0} \, \frac{1}{s} \, e^{jkz' \cos\beta_0}$$

with

$$s = \sqrt{x^2 + y^2 + (z - z')^2}$$

using the geometry illustrated in Figure 16. Therefore,

$$E_\theta^d = e^{-j\frac{3\pi}{4}} \sqrt{\frac{k}{2\pi}} \, E_z^i(z_s') D_s^* \, \frac{\sin\theta(z')}{\sin\beta_0} \, \frac{1}{s} \, e^{jkz'\cos\beta_0}$$

$$* \sqrt{\frac{s}{\sin^2\beta_0}} \, e^{-jks} \, e^{-jkz'\cos\beta_0} \, e^{-j\frac{\pi}{4}}$$

which reduces to

$$E_\theta^d = -\frac{E_z^i(z_s')}{\sin\beta_0} \, D_s^* \, \frac{e^{-jks}}{\sqrt{s}} \quad .$$

The above equation checks with (13a) in that $\hat\theta$ is in the $-\hat z$ direction and secondly

$$\frac{D_s^*}{\sin\beta_0} = D_s .$$

Returning to Equation (15) and using the fact that in the far field:

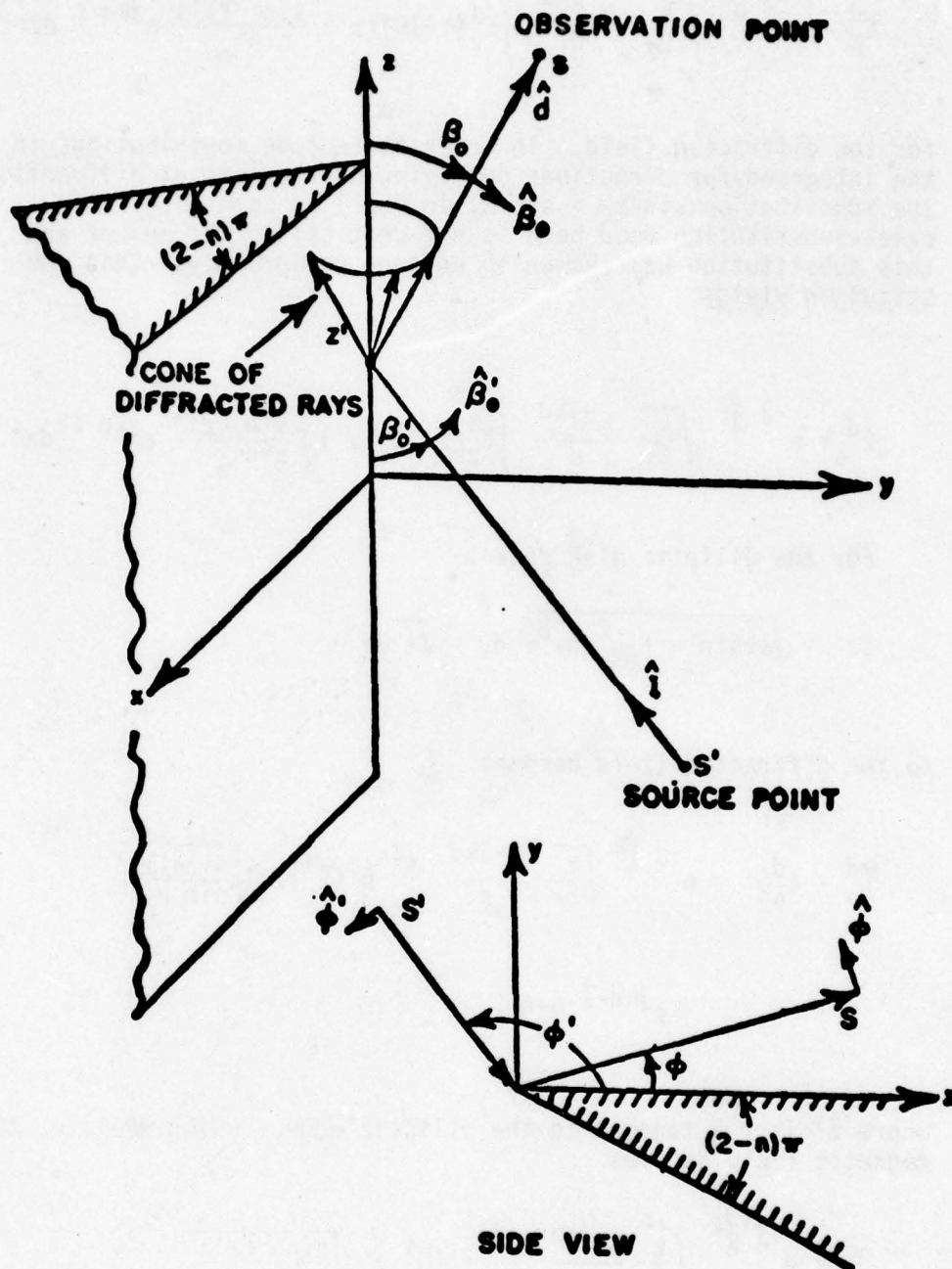$$s = d - \hat d \cdot \vec\ell ,$$

it follows that

38

Figure 16. Geometry for three-dimensional wedge diffraction problem.

39

$$E_\theta^d = e^{-j\frac{3\pi}{4}} \sqrt{\frac{k}{2\pi}} \frac{e^{-jkd}}{d} \int E_z^i(z')D_s^*(z') \frac{\sin\theta\,(z')}{\sin\beta_0} e^{jk\hat{d}\cdot\hat{\ell}}\, dz'$$

for the diffracted field. In order to include contributions in the integrand for directions not lying on the cone of diffraction the substitution $\sin^2\beta_0 = \sin\beta_0 \sin\theta(z')$ is used [15]. The exact substitution used here is not critical to the answer and this substitution was chosen to enforce reciprocity. This substitution yields:

$$E_\theta^d = e^{-j\frac{3\pi}{4}} \sqrt{\frac{k}{2\pi}} \frac{e^{-jkd}}{d} \int E_z^i(z')D_s^*(z') \sqrt{\frac{\sin\theta(z')}{\sin\beta_0}}\, e^{jk\hat{d}\cdot\hat{\ell}}\, dz'.$$

For the elliptic disk case

$$dz' = \sqrt{a^2\sin^2 v + b^2\cos^2 v}\; dv = \sqrt{\cdot}\; dv$$

so the diffracted field becomes

$$\vec{E}_e^d = E_\theta^d \hat{\theta}' = e^{-j\frac{3\pi}{4}} \sqrt{\frac{k}{2\pi}} \frac{e^{-jkd}}{d} \int_0^{2\pi} \hat{\theta}'\,(\vec{E}^i\cdot\hat{z}')\sqrt{\frac{\sin\theta(z')}{\sin\beta_0}}$$

$$\ast\, e^{jk\hat{d}\cdot\vec{\ell}}\, D_s^*\, \sqrt{\cdot}\; dv$$

where $\hat{z}'$ is the tangent to the elliptic edge. Using duality, the magnetic field becomes

$$\vec{H}_m^d = e^{-j\frac{3\pi}{4}} \sqrt{\frac{k}{2\pi}} \frac{e^{-jkd}}{d} \int_0^{2\pi} \hat{\theta}'\,(\vec{H}^i\cdot\hat{z}')\sqrt{\frac{\sin\theta\,(z')}{\sin\beta_0}}$$

$$\ast\, e^{jk\hat{d}\cdot\vec{\ell}}\, D_h^*\, \sqrt{\cdot}\; dv\ .$$

40

In the far field

$$\vec{E} \times \vec{H} = \frac{|E|^2}{z_o} \hat{d}$$

and

$$\vec{E} = z_o \vec{H} \times \hat{d}$$

which implies

$$\vec{E}_m^d = -e^{-j\frac{3\pi}{4}} \sqrt{\frac{k}{2\pi}} \frac{e^{-jkd}}{d} \int_0^{2\pi} \hat{\phi}(z_o \vec{H}^i \cdot \hat{z}') \sqrt{\frac{\sin\theta \ (z')}{\sin \beta_o}}$$

$$* \ e^{jk\hat{d}\cdot\vec{\ell}} \ D_h^* \ \sqrt{\cdot} \ dv \quad .$$

Also

$$z_o \vec{H}^i = \hat{d} \times \vec{E} = -E_\phi^i \cdot \hat{\theta}' + E_\theta^i \cdot \hat{\phi}' \quad .$$

Therefore

$$\vec{E}_m^d = -e^{-j\frac{3\pi}{4}} \sqrt{\frac{k}{2\pi}} \frac{e^{-jkd}}{d} \int_0^{2\pi} \hat{\phi}'[(-E_\phi^i\hat{\theta}+E_\theta^i\hat{\phi})\cdot\hat{z}']$$

$$* \sqrt{\frac{\sin\theta \ (z')}{\sin \beta_o}} \ e^{jk\hat{d}\cdot\vec{\ell}} \ D_h^* \ \sqrt{\cdot} \ dv \quad .$$

The D_s^* and D_h^* diffraction coefficients are two-dimensional diffraction coefficients computed by assuming a straight edge which is tangent to the elliptic edge at the integration point. D_s^* and D_h^* are computed using Equation (5) with $\sin\beta_o$ set equal to unity which implies $L = |\vec{\ell}|$.

41

The above equations for E_d^s and E_d^h are numerically integrated using the following technique:

$$\int_0^{2\pi} f(x)dx = \int_0^{2\pi} M(x)e^{j\phi(x)}dx = \sum_{\substack{x_o=0 \\ \text{in steps} \\ \text{of } \Delta x}}^{2\pi} \int_{x_o-\frac{\Delta x}{2}}^{x_o+\frac{\Delta x}{2}} M(x)e^{j\phi(x)}dx$$

where $M(x)$ and $\phi(x)$ are the magnitude and phase of $f(x)$, respectively. Over the interval Δx, the magnitude is assumed constant and the phase is assumed to be linear. The integral now becomes

$$\int_0^{2\pi} f(x)dx \approx \sum_{\substack{x_o=0 \\ \text{in steps} \\ \text{of } \Delta x}}^{2\pi} f(x_o)\ \Delta x\ \frac{\sin\left(\frac{a\Delta x}{2}\right)}{\left(\frac{a\Delta x}{2}\right)}$$

where

$$a = \frac{d[\phi(x)]}{dx}\Bigg|_{x_o} \approx \frac{\phi(x_o+\Delta x)-\phi(x_o-\Delta x)}{2\Delta x}\ .$$

If Δx is one degree, the integral can be reduced to

$$\int_0^{2\pi} f(x)dx \approx \frac{\pi}{180} \sum_{x_o=0^\circ}^{180^\circ} f(x_o)\ \frac{\sin A}{A}$$

where

$$A = \frac{\phi(x_o+1^\circ)-\phi(x_o-1^\circ)}{4}\ .$$

The equivalent current solution is only truly valid in the vicinity of a caustic. This method can, however, yield good results in other scatter directions due to the stationary phase nature of the integrand at points of diffraction. One region where this method is not usually valid is in the area around the

42

incident and reflected shadow boundaries. This effect can be
seen by examining the problem illustrated in Figure 17 and also
can be seen as a discontinuity in the integrand of the equivalent
current solution as shown in Figure 18, where the reflected shadow
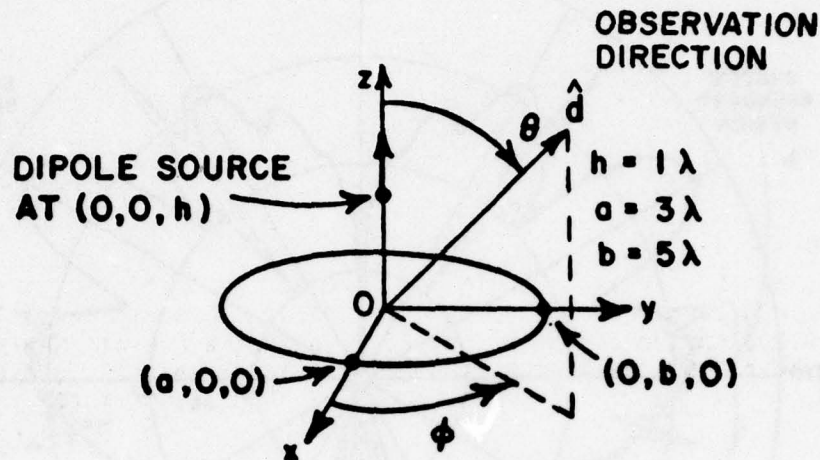boundary is at 78.7°.

Figure 17(a). Dipole off an elliptic disc.

A computational problem associated with the equivalent
current solution is that it requires integration around the
elliptic edge for each observation direction. This requires a
large amount of computer time when compared with the GTD four point
diffraction solution which requires calculation at a maximum of
four points along the rim.

Since the four point diffraction solution and the equivalent
current solution fail for different reasons, the discontinuities
in the pattern caused by the diffracted field will, in general,
appear in different regions of the pattern. Thus, the two methods
may be combined, in most cases, to yield a smooth pattern which
avoids the difficulties associated with each individual method.
One case where this will not usually yield a smooth pattern is
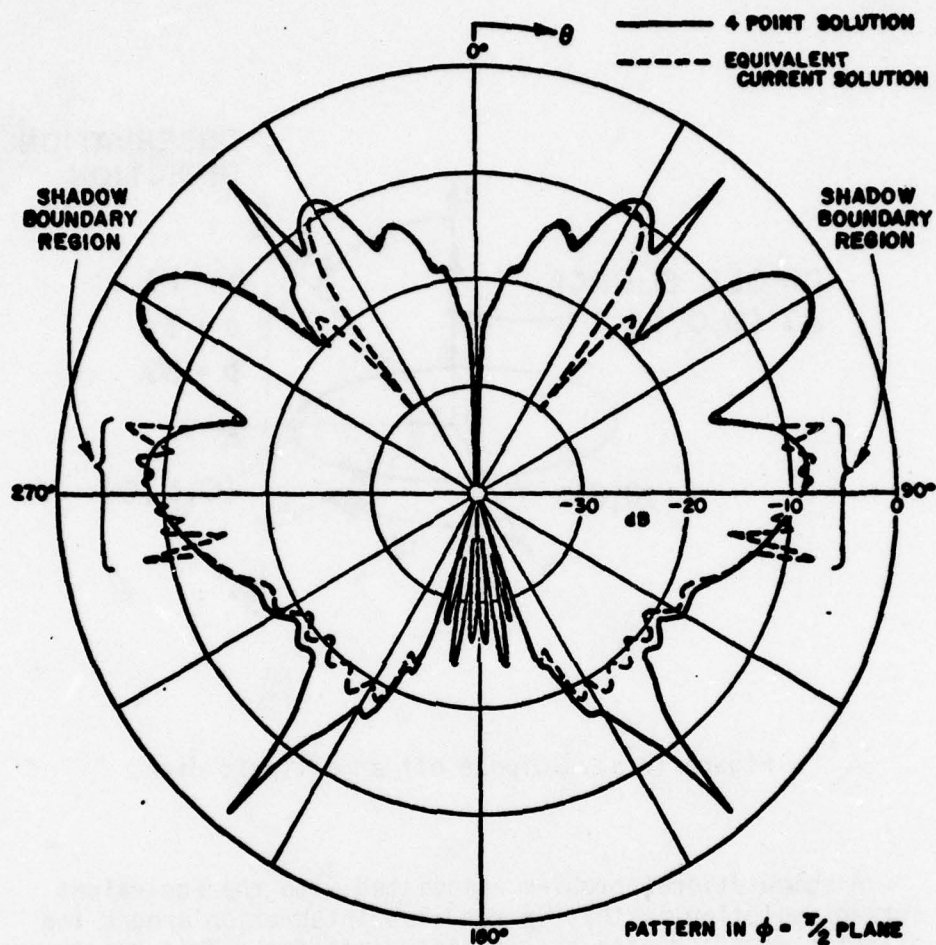when the caustic and a shadow boundary coincide.

43

Figure 17(b). Radiation pattern of the configuration in
Figure 17(b); the sharp peaks in the 4-point
solution occur at the pseudo-caustics where
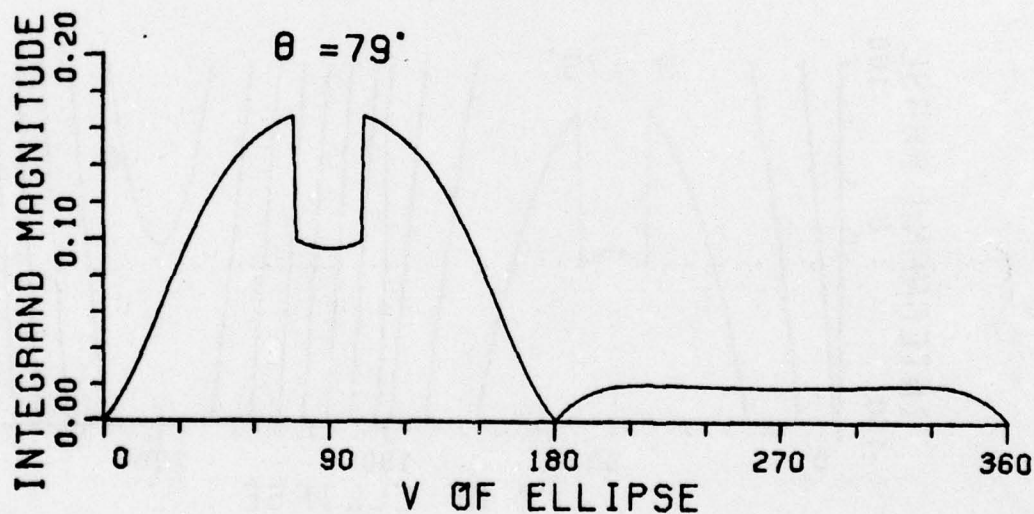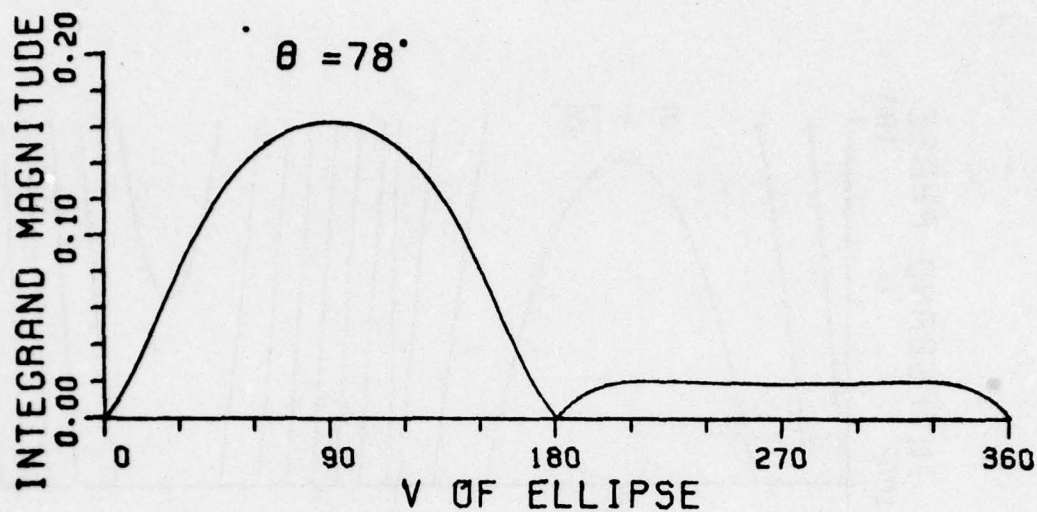the equivalent current solution must be
employed.

44

Figure 18(a). Discontinuties occuring in the integrand
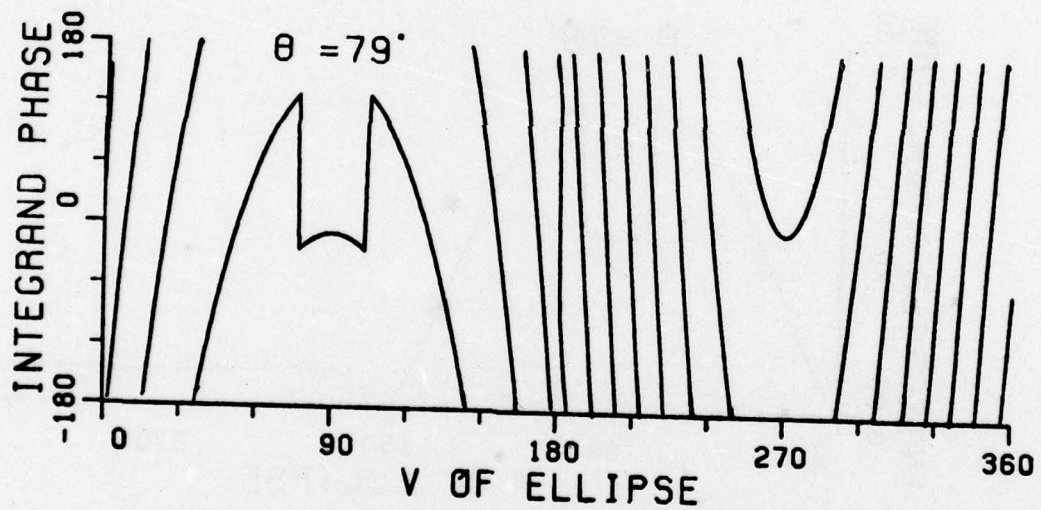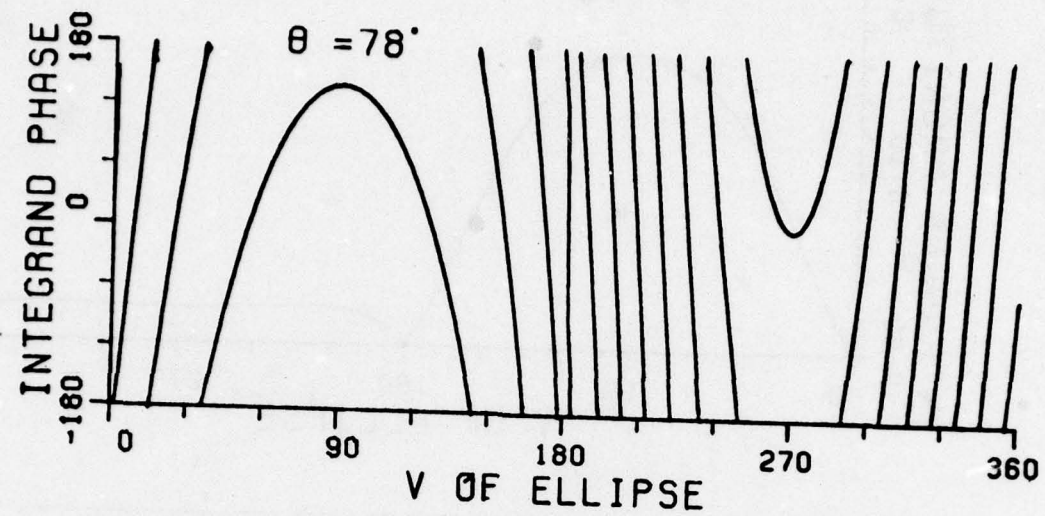magnitude of the equivalent current
solution near the shadow boundary.

Figure 18(b). Discontinuities occuring in the integrand phase of the equivalent current solution near this shadow boundary.

The four point diffraction solution is used whenever possible since it is the more numerically efficient. The equivalent current solution is used to correct the caustic and pseudo-caustic problems associated with the four point diffraction solution.

The mechanism chosen to switch between the two methods is based upon the stationary phase nature of the integrand in the equivalent current solution in the neighborhood of a diffraction point. The axial caustic problem, associated with the geometry illustrated in Figure 13, is apparent from the phase of the integrand as seen in Figure 19. Note that the phase is constant at the caustics ($\theta=0$) and has a broad stationary phase peak in the vicinity of the caustic. The phase of the integrand is shown in Figure 20 for the pseudo-caustic case of Figure 14b. Four distinct phase extremums are seen when $\theta=45°$ which correspond to the four diffraction points at $v=32°$, $90°$, $148°$, and $270°$. As the observation angle changes to $\theta=57°$, three of the four diffraction points merge into one at $v = 90°$. The stationary phase peak at this point becomes very broad as seen in Figure 20. In both the caustic and pseudo-caustic cases, it is noted that the width of these extremums is a good indication that a caustic is present and the equivalent current solution should be implemented.

As a result of the above arguments, the second derivitive of the phase at the diffraction points yields a good measure of the width of these stationary phase peaks, such that it can be used to determine the switching procedure. The phase of the integrand can be specified in a simplified form by the phase of the diffracted field at the diffraction point v_i. Thus

$$n_i = -|\vec{I}| + \hat{d} \cdot \vec{R}$$

where

$$\vec{R} = a \cos v_i \, \hat{x} + b \sin v_i \, \hat{y}$$

and

$$\vec{I} = \vec{R} - \vec{x}_s$$

using the geometry illustrated in Figure 21. The second derivitive is computed numerically by

$$\dot{n}_i = \frac{n_{i+1} - n_{i-1}}{2 \Delta v}$$

47

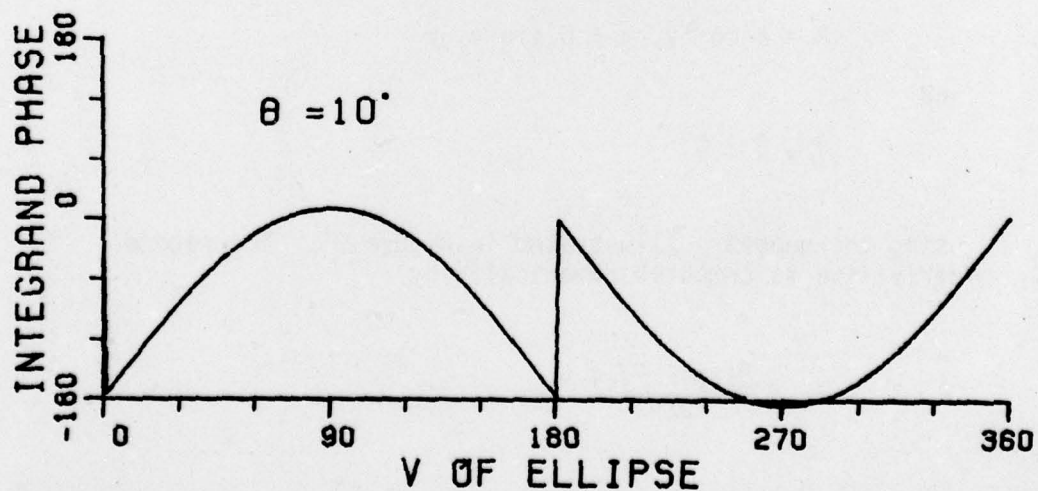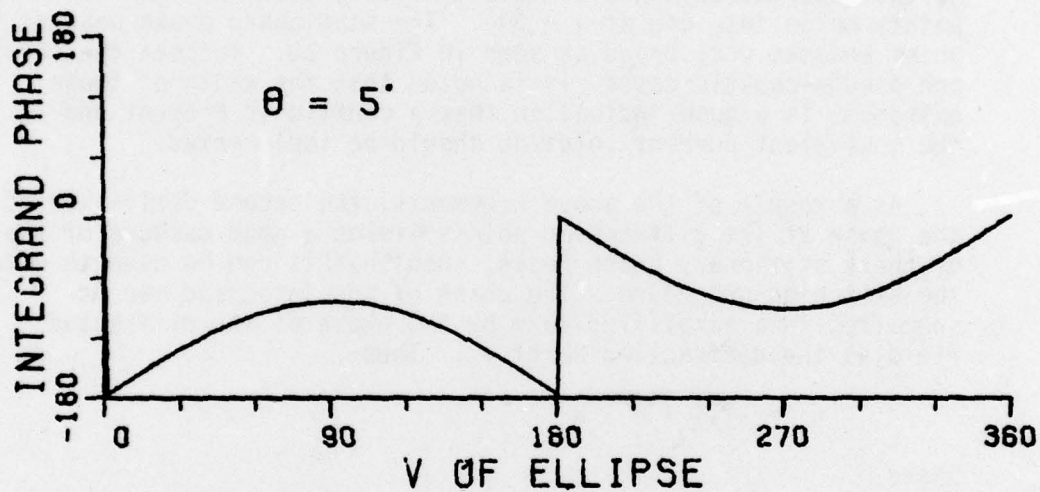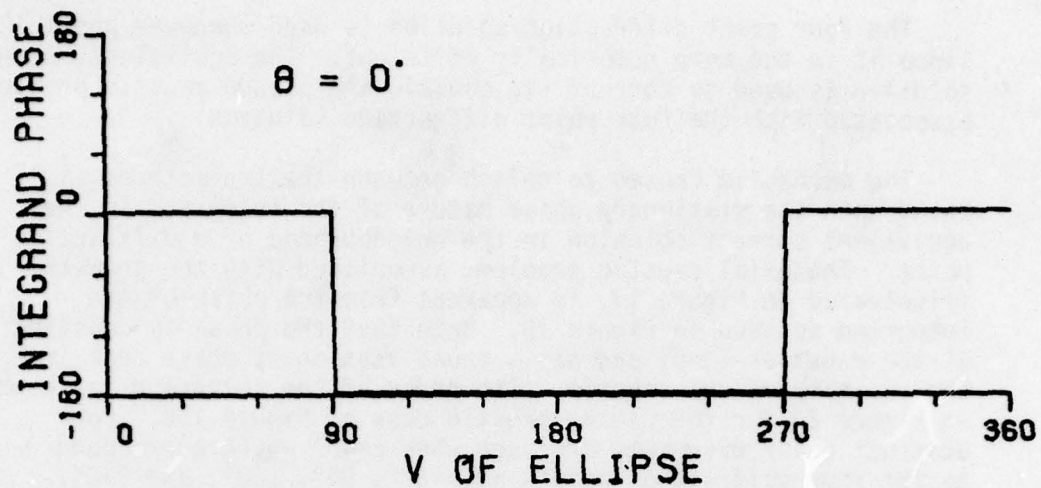Figure 19. Phase plot of equivalent current integrand near an axial caustic at 0° (a=b=3λ).

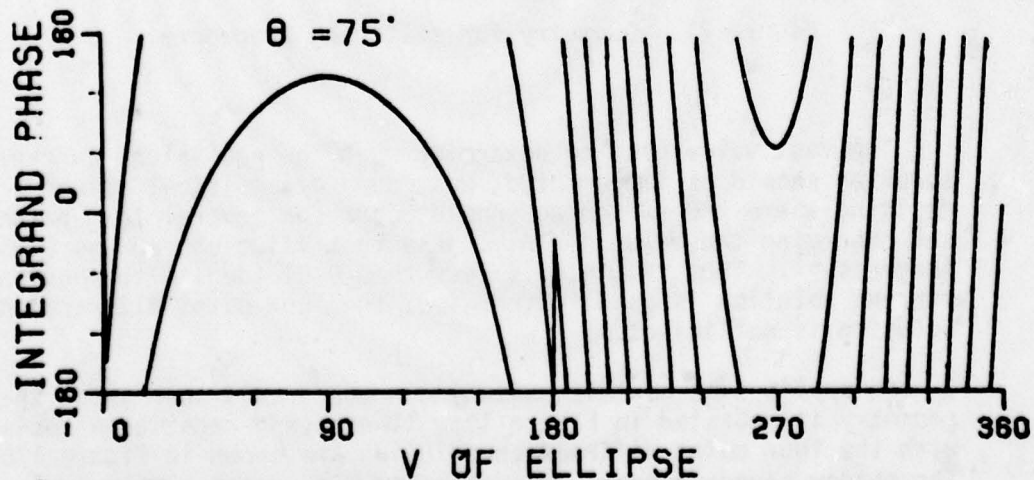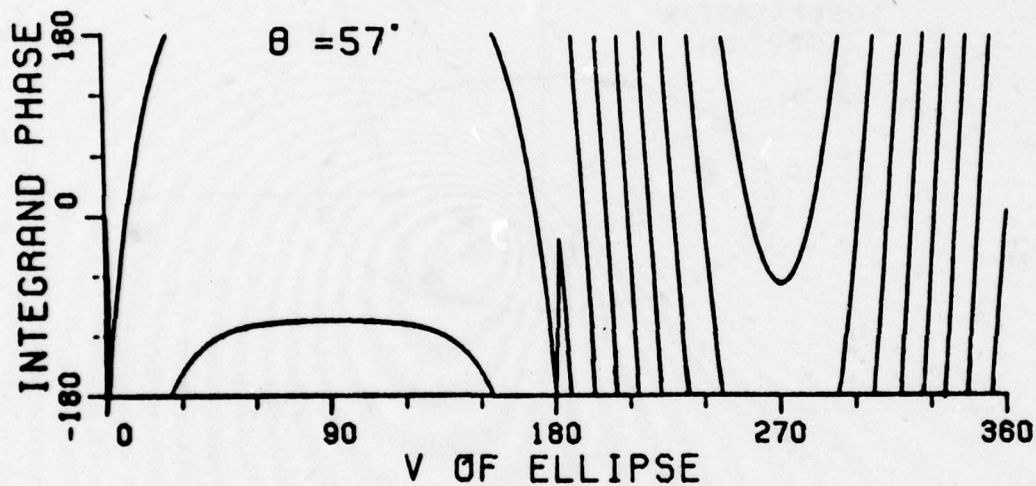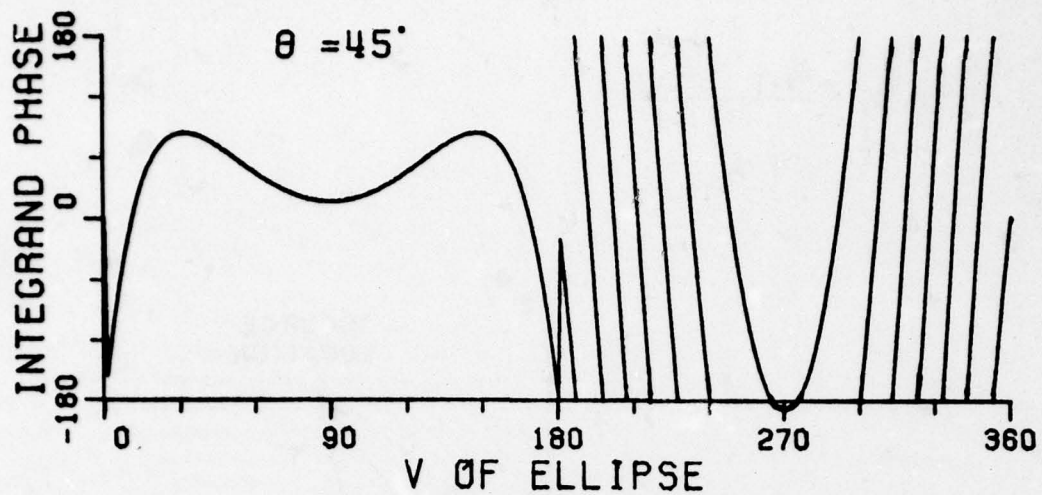Figure 20. Phase plot of equivalent current integrand near a pseudo-caustic at 57° (a=2λ, b=5λ).

49

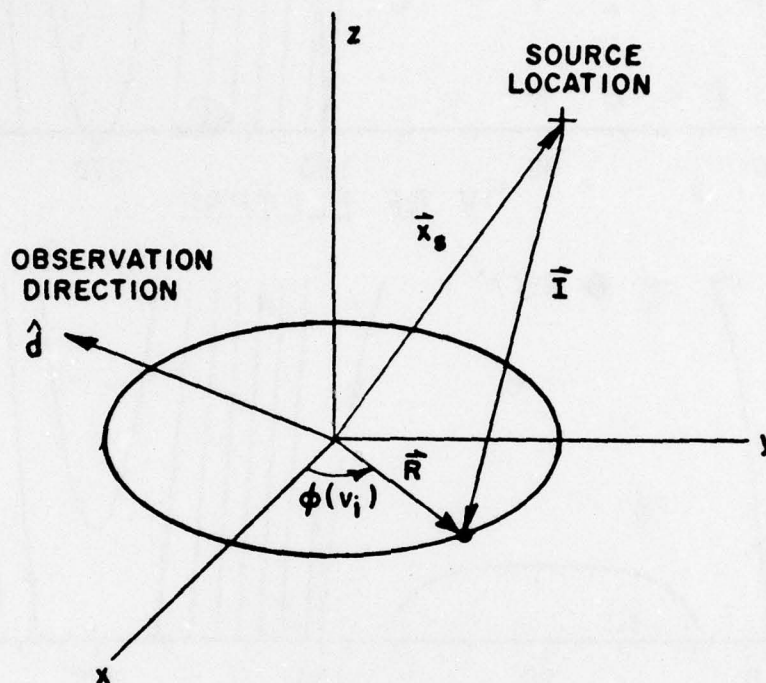$$\dot{n}_i = \frac{\dot{n}_{i+1} - \dot{n}_{i-1}}{2\Delta v} \quad .$$

Figure 21. Geometry for switching procedure.

The test value used to determine when the equivalent current solution should be implemented, was found by empirical methods, i.e., deciding where the switching should occur for several test patterns and observing the value of $\dot{n}_i$. The test value chosen was 0.01 (degrees)$^{-1}$. Thus if $|\dot{n}_i|$ is less than 0.01 (deg)$^{-1}$ the equivalent current solution is used. Otherwise, the four point diffraction solution is sufficient.

An application of this switching procedure is seen using the geometry illustrated in Figure 17a. The pseudo-caustics associated with the four point diffraction solution are shown in Figure 17b. The shadow boundary problems associated with the equivalent

current solution can also be seen in Figure 17b. The combined
solution avoids both of these difficulties by employing the
equivalent current solution only in the pseudo-caustic regions.
The combined solution is shown in Figure 22.

The accuracy of the combined solution can be demonstrated
by comparison with measured results. In Figure 23a the axial
caustics associated with the GTD four point diffraction solution
is observed at $\theta=0°$ and $180°$. The combined solution which cor-
rects these caustics via equivalent current is seen in the same
figure and is compared with measured results taken on a 3λ circular
disk [16] as shown in Figure 23b. The comparison between measured
results and the combined solution for the pseudo-caustic case
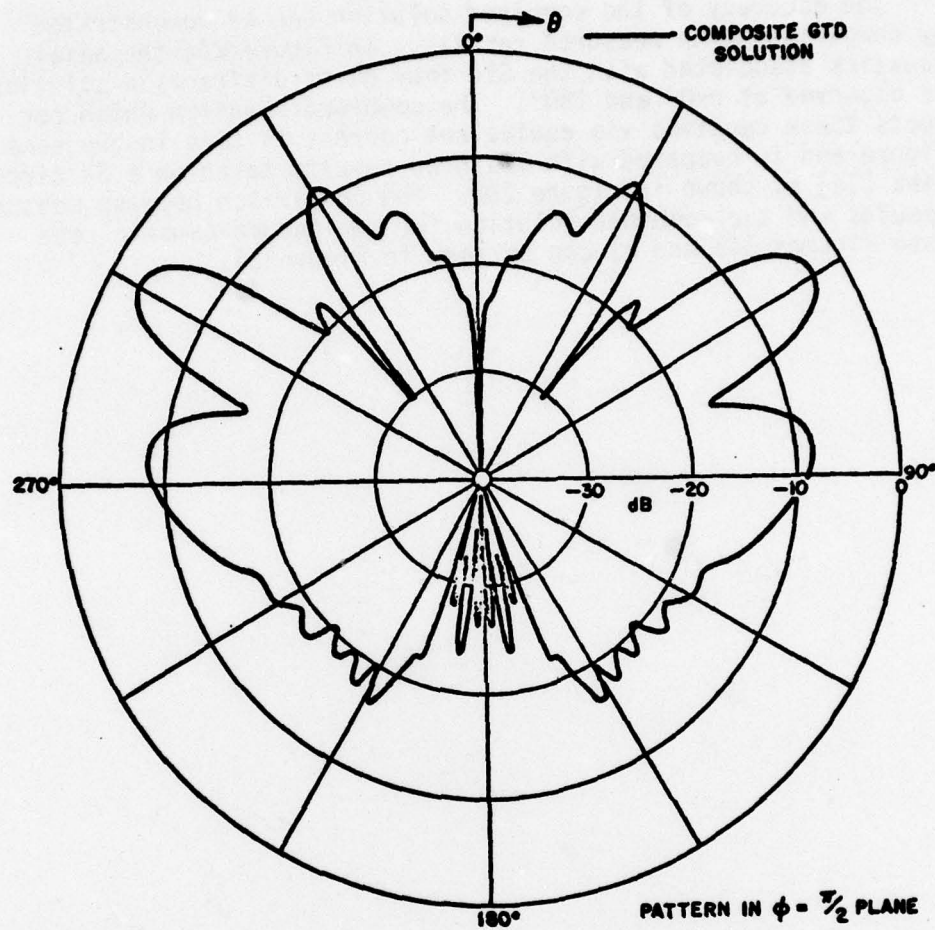(see Figures 14a and b) can be seen in Figure 24.

Figure 22. The composite 4-point + equivalent current solution corresponding to Figure 17(a).
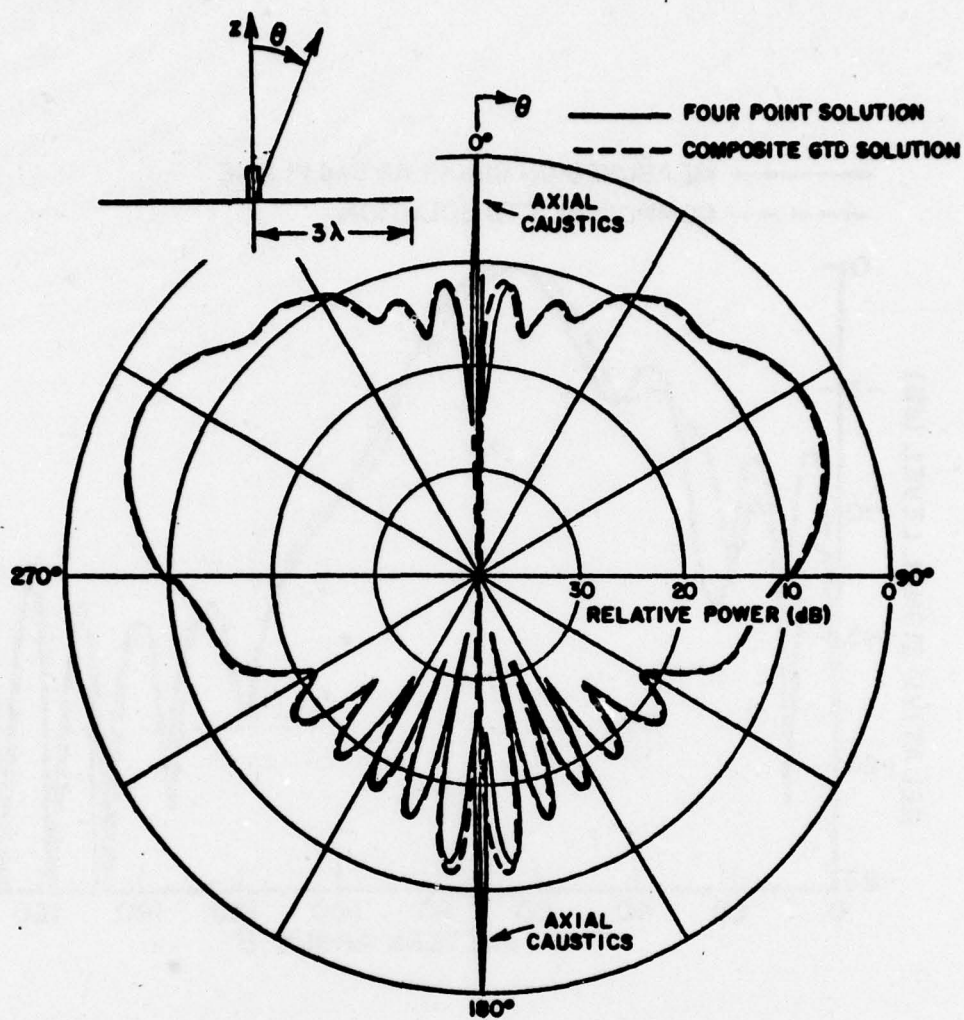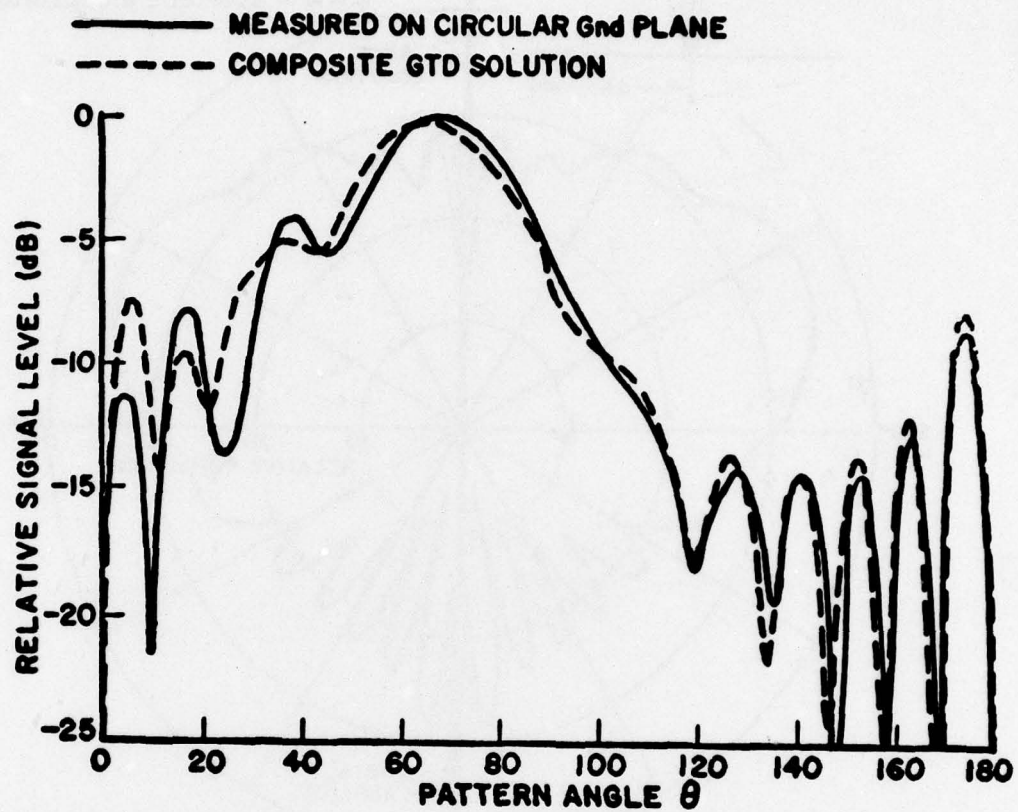
Figure 23(a). Axial caustics on a 3λ circular disk.

Figure 23(b). Comparison of combined solution with measured results on a 3λ circular disk.
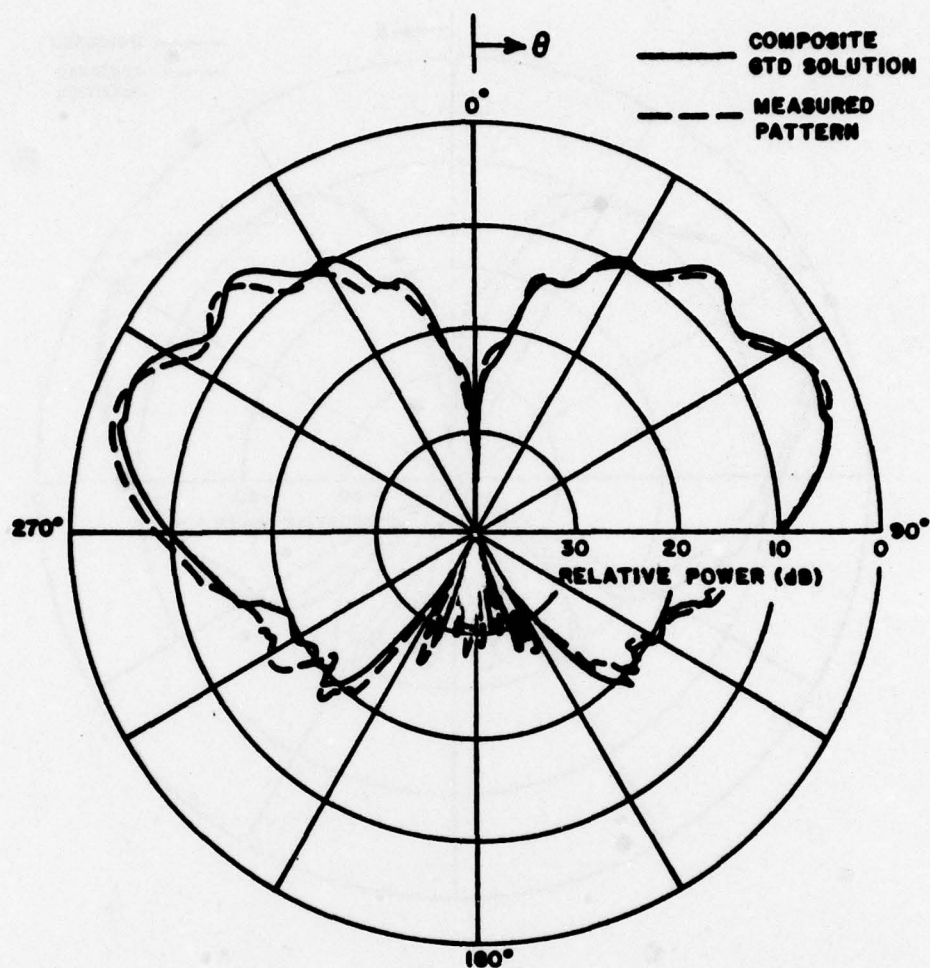
Figure 24(a). Composite solution for E-theta radiation in
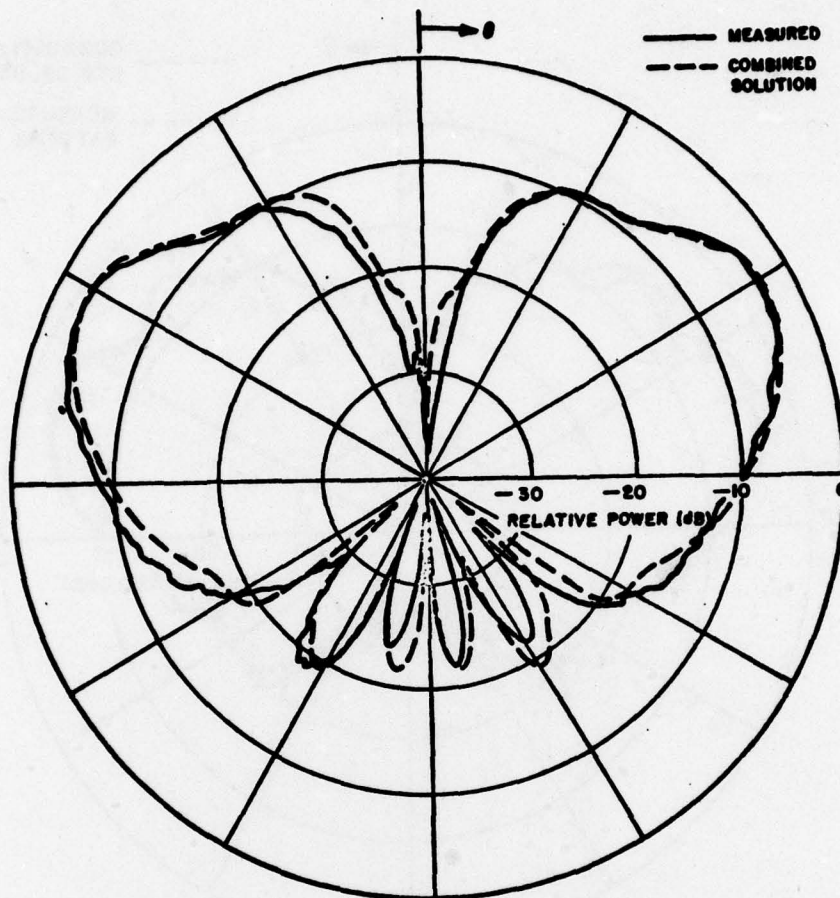y-z plane corresponding to Figure 14(a).

Figure 24(b). E-theta radiation pattern for φ=45°
corresponding to Figure 14(a).

CHAPTER V
SUMMARY AND CONCLUSIONS

The object of this study has been to analyze the radiated field of an antenna mounted near an elliptic disk at high frequency. The basic approach used in this study to analyze the scattering by an elliptic disk was to employ the Geometrical Theory of Diffraction discussed briefly in Chapter II. The incident, reflected, and diffracted fields were discussed in Chapter III. The diffracted field was described using the GTD four point diffraction method.

In Chapter IV the method of equivalent currents was employed to correct for caustics and pseudo-caustics associated with the GTD four point diffraction solution. An empirical switching procedure was introduced in order to apply the equivalent current solution whenever caustics occur in the four point diffraction solution.

The combined solution for the elliptic disk was compared with measured results on a circular and elliptic disk to verify its accuracy.

The equivalent current solution has been shown to be an effective method of removing caustics associated with the GTD four point diffraction solution on the elliptic disk. The combined elliptic disk solution using the GTD four point diffraction solution with the equivalent current solution in the caustic regions, can be used effectively to predict patterns of sources located near an elliptic disk.

The elliptic disk solution is useful in predicting antenna patterns for antenna located on circular or elliptic gorund planes. The elliptic disk can also be used as an approximation to an arbitrary cross-section flat plate or as an endcap for an elliptic cylinder. The elliptic cylinder model can be used to model structures on an aircraft such as the fuselage, engines, and stores or structures on ships such as masks, stores, etc.

57

REFERENCES

[1] Keller, J. B., "Geometrical Theory of Diffraction," Jour. Optical Soc. Amer., 52 (February 1962), pp. 116-130.

[2] Kouyoumjian, R. G. and Pathak, P., "A Uniform Geometrical Theory of Diffraction for an Edge of a Perfectly Conducting Surface," Proc. of the IEEE, Vol. 62, No. 11. November, 1974, pp. 1448-1461.

[3] Ryan, C. E., Jr., and Peters, L., Jr., "Evaluation of Edge-Diffracted Fields Including Equivalent Currents for the Caustic Regions," IEEE Trans. on Antennas and Propagation Comm., Vol. AP-7, pp. 292-299, May 1969. (see also correction: Vol. AP-8, p. 275, March 1970.)

[4] Walter, C. H., Traveling Wave Antennas, Dover Publications, Inc., New York, 1970, pp. 15-16.

[5] Sommerfeld, A., Optics, Academic Press, Inc., New York, 1954, pp. 245-265.

[6] Keller, J. B., op. cit.

[7] Rudduck, R. C., "Application of Wedge Diffraction to Antenna Theory," Report 1691-13, 30 June 1965, The Ohio State University ElectroScience Laboratory, Department of Electrical Engineering; prepared under Grant NSF-338 for National Aeronautics and Space Administration, Washington, D. C. Also published as NASA Report CR-372.

[8] Pauli, W., "An Asymptotic Series for Functions in the Theory of Diffraction of Light," Phys. Rev., 54 (1 December 1938), pp. 924-931.

[9] Hutchins, D. L., and Kouyoumjian, R. G., "A New Asymptotic Solution to the Diffraction by a Wedge," URSI 1967 Spring Meeting, Ottawa, Canada, pp. 154-155.

[10] Hutchins, D. L., "Asymptotic Series Describing the Diffraction of a Plane Wave by a Two-Dimensional Wedge of Arbitrary Angle," Ph.D. Dissertation, The Ohio State University, Department of Electrical Engineering, 1967.

[11] Pathak, P. H., and Kouyoumjian, R. G., "The Dyadic Diffraction Coefficient for a Perfectly Conducting Wedge," Scientific Report No. 5, Report 2183-4, 5 June 1970, The Ohio State University ElectroScience Laboratory, Department of Electrical Engineering; prepared under Contract AF19(628)-5929 for Air Force Cambridge Research Laboratories. (AFCRL-69-0546) (AD 707821)

[12] Kouyoumjian, R. G. and Pathak, P., "A Uniform Geometrical Theory of Diffraction for an Edge of a Perfectly Conducting Surface," op. cit.

[13] Ryan, C. E., Jr., and Peters, L., Jr., op. cit.

[14] Papoulis, A., The Fourier Integral and Its Applications, McGraw-Hill, New York, 1962, pp. 139-143.

[15] Knott, E. F. and Senior, T. B. A., "Comparison of Three High-Frequency Diffraction Techniques," Proc. of the IEEE, Vol. 62, No. 11, November, 1974, pp. 1468-1474.

[16] Lopez, A. R., "The Geometrical Theory of Diffraction Applied to Antenna Pattern and Impedance Calculations," IEEE Transactions on Antennas and Propagation, Vol. AP-14, No. 1, January 1966, p. 40.